Precise determination of the long-time asymptotics of the diffusion spreadability of two-phase media

Shaobing Yuan
Department of Chemistry and Princeton Institute for the Science and Technology of Materials, Princeton University, Princeton, New Jersey 08544, USA

Salvatore Torquato*
Department of Chemistry, Department of Physics, Princeton Center for Theoretical Science, Princeton Institute for the Science and Technology of Materials, and Program in Applied and Computational Mathematics, Princeton University, Princeton, New Jersey 08544, USA

(Received 15 February 2026; accepted 27 May 2026; published 23 June 2026)

The time-dependent diffusion spreadability $\mathcal{S}(t)$ is a powerful dynamical probe of the microstructure of two-phase heterogeneous media across length scales [S. Torquato Phys. Rev. E **104**, 054102 (2021)]. The spreadability can be exactly represented as a certain functional of the spectral density $\tilde{\chi}_v(\mathbf{k})$, where $\mathbf{k}$ is the wave vector. Experimentally, it is intimately related to nuclear magnetic resonance (NMR) measurements in fluid-saturated media. The short-, intermediate-, and long-time behavior of the spreadability reflects structural features at small, intermediate, and large length scales, respectively. It has been shown that when the spectral density takes the power-law form $\tilde{\chi}_v(\mathbf{k}) \sim |\mathbf{k}|^\alpha$ as the wave number $|\mathbf{k}|$ tends to zero, the normalized excess spreadability $\mathcal{I}^{\rm ex}(t)$ [proportional to $\mathcal{S}(\infty) - \mathcal{S}(t)$] scales as $\mathcal{I}^{\rm ex}(t) \sim t^{-\frac{d+\alpha}{2}}$ in the long-time limit $t \to \infty$, enabling one to determine the infinite-wavelength scaling exponent α. An algorithm that allows one to reliably extract the exponent α from long-time spreadability data was previously devised [H. Wang and S. Torquato, Phys. Rev. Appl. **17**, 034022 (2022)]. In this paper, we further improve this procedure to obtain α even more accurately by incorporating higher-order correction terms to the long-time asymptotics and by utilizing analyticity properties of $\tilde{\chi}_v(k)$ at the origin. We illustrate our procedure by analyzing hyperuniform ($\alpha > 0$), typical nonhyperuniform ($\alpha = 0$), and antihyperuniform ($-d < \alpha < 0$) models of two-phase media. In addition, by combining the large-t asymptotic expansion of $\mathcal{I}^{\rm ex}(t)$ with the small-t expansion, we have devised a two-point Padé approximant to accurately approximate $\mathcal{I}^{\rm ex}(t)$ for all t with just a few parameters. Our findings facilitate the characterization of the microstructure of two-phase media across length scales as obtained from numerical spreadability data or experimental data obtained from NMR relaxation measurements. Our work can also be applied in the inverse design of two-phase microstructures with targeted spreadability behaviors.

DOI: 10.1103/9vyf-br6d

I. INTRODUCTION

Time-dependent interphase diffusion processes in heterogeneous media play an important role in a myriad of contexts, including MRI [1–5], geological media [6], biological cells [7], chemical catalysis [8], material design [9], and drug delivery [10]. Mutliphase heterogeneous media are ubiquitous in nature and synthetic materials; examples include, among others, composites, foams, gels, porous media, and biological tissues [6,11–14]. The effective properties of heterogeneous media as a whole, including transport properties like the effective conductivity, depend on and reflect the underlying microstructure, which is fully statistically characterized by an infinite set of n-point correlation functions [6,15,16] defined in Sec. II.

Torquato developed the concept of the time-dependent *diffusion spreadability* $\mathcal{S}(t)$ [17], making a direct link between the interphase diffusion problem and the microstructure of the system across length scales. Consider the time-dependent mass transfer of a solute in a two-phase medium where phases 1 and 2 occupy volume fractions ϕ_1 and ϕ_2, respectively, under a diffusion coefficient D that is constant at any time t in either phase, such that all of the solute is uniformly distributed in phase 2 at an initial time $t = 0$. The mass fraction of the total solute that has diffused from phase 2 to phase 1 at time t is defined as the *diffusion spreadability* $\mathcal{S}(t)$. Torquato provided the exact formula for $\mathcal{S}(t)$ in any dimension d in terms of the autocovariance function $\chi_v(\mathbf{r})$ in direct space (generalizing Prager's 3D solution in direct space [18]), or equivalently, the spectral density $\tilde{\chi}_v(\mathbf{k})$ in Fourier space, as follows:

$$\begin{aligned}\mathcal{I}^{\rm ex}(t) &\equiv 1 - \frac{\mathcal{S}(t)}{\mathcal{S}(\infty)} = \phi_1^{-1}[\mathcal{S}(\infty) - \mathcal{S}(t)] \\ &= \frac{1}{(4\pi Dt)^{d/2}} \int_{\mathbb{R}^d} \frac{\chi_v(\mathbf{r})}{\phi_1\phi_2} e^{-\frac{r^2}{4Dt}} d\mathbf{r} \\ &= \frac{1}{(2\pi)^d} \int_{\mathbb{R}^d} \frac{\tilde{\chi}_v(\mathbf{k})}{\phi_1\phi_2} e^{-k^2Dt} d\mathbf{k}, \end{aligned} \tag{1}$$

where $\mathcal{S}(\infty) - \mathcal{S}(t)$ is called the *excess spreadability*, i.e., the spreadability in excess of its infinite-time limit

*Contact author: torquato@electron.princeton.edu

 ©2026 American Physical Society

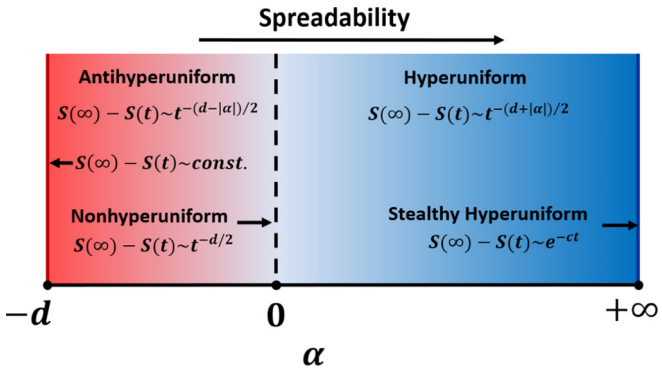


FIG. 1. Phase diagram that schematically shows the spectrum of spreadability regimes in terms of the long-distance scaling exponent α. As α increases from the extreme antihyperuniform limit of $\alpha \to -d$, the spreadability decay rate at long times decays faster, that is, the excess spreadability follows the inverse power law $1/t^{(d+\alpha)/2}$, except when $\alpha \to \infty$, which corresponds to stealthy hyperuniform media with an exponentially fast decay rate. This figure is reproduced from the one presented in Ref. [17].

$\mathcal{S}(\infty) = \phi_1$, and $\mathcal{I}^{\rm ex}(t)$ is the *normalized excess spreadability*, which monotonically decreases from 1 to 0 as time t goes from 0 to ∞. This is one of the rare cases where the effective transport property is exactly determined by up to two-point correlations rather than the whole infinite set of correlation functions. Equation (1) implies that small-, intermediate-, and long-time behaviors of $\mathcal{S}(t)$ are equivalent to small-, intermediate-, and large-scale features of the microstructure [17,19].

Torquato [17] showed that, assuming a power-law scaling of the spectral density $\tilde{\chi}_v(\mathbf{k}) \sim B|\mathbf{k}a|^{\alpha}$ at the infinite-wavelength limit $|\mathbf{k}| \to 0$, the long-time excess spreadability scales as

$$\mathcal{S}(\infty) - \mathcal{S}(t) = \frac{B\Gamma\left(\frac{d+\alpha}{2}\right)}{(4\pi)^{d/2}\Gamma(d/2)\phi_2}(Dt/a^2)^{-\frac{d+\alpha}{2}} + o\left[(Dt/a^2)^{-\frac{d+\alpha}{2}}\right], \quad t \to \infty, \tag{2}$$

where a is some characteristic heterogeneity length scale of the two-phase random media. The value of the exponent α distinguishes nonhyperuniform systems ($\alpha \leqslant 0$) from hyperuniform ones ($\alpha > 0$). Disordered hyperuniform systems are of particular importance because of their anomalous suppression of volume fraction fluctuations relative to ordinary disordered media [20–22], which endows them with novel properties of fundamental interest and practical use, relevant contexts including glass formation [23–27], maximally random jammed sphere packings [28–34], photonic and phononic materials [35–41], mathematics [42–48], biology and ecology [49–53], self-organization [54–56], disordered classical ground states [57–63], and quantum systems [64–71].

Figure 1 schematically shows the "phase diagram" of spreadability regimes in terms of the exponent α [17]. The long-time excess spreadability for antihyperuniform media ($-d < \alpha < 0$) has the slowest decay among all translationally invariant media. A long-time decay rate of $\mathcal{I}^{\rm ex}(t) \sim t^{-d/2}$ corresponds to a "typical" nonhyperuniform medium in which the spectral density is a bounded positive number at the origin, i.e., $\alpha = 0$. The excess spreadability for nonstealthy hyperuniform media ($0 < \alpha < \infty$) has the aforementioned power-law decay $\mathcal{I}^{\rm ex}(t) \sim t^{-(d+\alpha)/2}$. The limit $\alpha \to +\infty$ corresponds to media in which the decay rate of $\mathcal{I}^{\rm ex}(t)$ is faster than any inverse power law, which is the case for stealthy hyperuniform media, disordered or ordered [17]. The reader is referred to Sec. II for terminology.

The concept of diffusion spreadability is intimately related to magnetic relaxation measurements, as demonstrated by Torquato [17]. He identified precise mappings between the long-time asymptotic formulas for the spreadability and the nuclear magnetic resonance (NMR) pulsed field gradient spin-echo (PFGSE) amplitude via a diffusion propagator that also only involves the two-point correlation function [72] as well as diffusion-weighted magnetic resonance imaging (dMRI) measurements in biological tissue [2,3]. Furthermore, Wilken *et al.* [73] showed that phase-separated DNA droplets spontaneously form hyperuniform structures and suggested that the long-time diffusion spreadability behaviors can be exploited in chemical reaction schemes analogous to those present in biomolecular condensates. To better model real experimental systems, Skolnick and Torquato [74] generalized the spreadability problem by considering different phase diffusion coefficients and showed that when time is rescaled by the effective diffusion coefficient D_e, the simulated spreadability for all times closely follows the spreadability curve for equal diffusion coefficients and hence is effectively controlled by the two-point correlation function only.

Apart from its connection to the NMR and other experiments, the spreadability is a powerful diagnostic to characterize the large-scale structure of both hyperuniform and nonhyperuniform media by determining the scaling exponent α. Such examples include the analysis of various hard particle packing problems [75–77], the conserved directed percolation problem [78], and certain quasicrystalline systems [79]. The spreadability offers a superior means to extract α accurately and robustly from fitting its long-time asymptotics compared to fitting noisy scattering data, since the spreadability can be regarded as a Gaussian smoothing of the spectral density, as indicated by Eq. (1), and is thus less susceptible to pointwise variations in spectral density $\tilde{\chi}_v(k)$ [75].

Wang and Torquato [19] developed a systematic spreadability fitting algorithm that enables one to reliably extract the scaling exponent α in the asymptotic power law (2) from the long-time data of $\mathcal{I}^{\rm ex}(t)$, which can be further improved to estimate α even more accurately. The precision of the Wang-Torquato algorithm depends on whether the true long-time behavior is achieved; the larger the time t, the closer one is to the asymptotic power law (2), and hence the more accurate is the estimate of the exponent α. Furthermore, since the residual $o[(Dt/a^2)^{-\frac{d+\alpha}{2}}]$ does not change the sign at large t, the fitting procedure inevitably leads to a systematic error in the value of the exponent α. In this paper, we demonstrate how we can enhance the fitting precision by incorporating higher-order terms in the large-t asymptotic expansion of $\mathcal{I}^{\rm ex}(t)$ in addition to exploiting the mathematical properties of $\tilde{\chi}_v(\mathbf{k})$ and $\chi_v(\mathbf{r})$. Additionally, we obtain two-point Padé approximants by combining the large-t fits of the asymptotic expansion of

$\mathcal{I}^{\rm ex}(t)$ with the small-t expansion, and show that they provide a good approximation of $\mathcal{I}^{\rm ex}(t)$ for all times t.

The paper is organized as follows. In Sec. II, we provide basic definitions and preliminaries. We then demonstrate the mathematical properties and the physical implications of the large-t asymptotic expansion of the spreadability $\mathcal{I}^{\rm ex}(t)$ (Sec. III). Section IV presents how the fitting is improved based on the theory. Its applications to a few representative models are shown in Sec. V. Finally, we discuss the implications of the results and conclude in Sec. VI.

II. BACKGROUND

A. Correlation functions

A two-phase random medium is a domain of space $\mathcal{V} \subseteq \mathbb{R}^d$ of volume V that is partitioned into two disjoint regions that make up $\mathcal{V}$: a phase 1 region $\mathcal{V}_1$ of volume fraction ϕ_1 and a phase 2 region $\mathcal{V}_2$ of volume fraction ϕ_2 [6]. The microstructure of a two-phase medium is fully statistically characterized by an infinite set of n-point correlation functions [6,15,16] defined by

$$S_n^{(i)}(\mathbf{x}_1, ..., \mathbf{x}_n) \equiv \langle \mathcal{I}^{(i)}(\mathbf{x}_1)...\mathcal{I}^{(i)}(\mathbf{x}_n)\rangle, \tag{3}$$

where $\mathcal{I}^{(i)}(\mathbf{x})$ is the *indicator function* for phase $i = 1, 2$ defined as

$$\mathcal{I}^{(i)}(\mathbf{x}) = \begin{cases} 1, & \mathbf{x} \in \mathcal{V}_i, \\ 0, & \mathbf{x} \notin \mathcal{V}_i, \end{cases} \tag{4}$$

for a given realization, and angular brackets denote an ensemble average. Physically, the value of $S_n^{(i)}(\mathbf{x}_1, ..., \mathbf{x}_n)$ corresponds to the probability of finding the vertices of a polyhedron located at $\mathbf{x}_1, ..., \mathbf{x}_n$ all in phase i. Assuming statistical translational symmetry, $S_n^{(i)}(\mathbf{x}_1, ..., \mathbf{x}_n)$ depends only on the relative positions, i.e., $S_n^{(i)}(\mathbf{x}_1, \mathbf{x}_2, ..., \mathbf{x}_n) = S_n^{(i)}(\mathbf{x}_{12}, ..., \mathbf{x}_{1n})$, where $\mathbf{x}_{ij} = \mathbf{x}_j - \mathbf{x}_i$. Particularly, we have $S_1^{(i)}(\mathbf{x}_1) = \langle \mathcal{I}^{(i)}(\mathbf{x}_1)\rangle = \phi_i$.

In this paper, our central focus is on the two-point correlation function $S_2^{(i)}(\mathbf{r})$, which exactly determines $\mathcal{I}^{\rm ex}(t)$ via formula (1). The *autocovariance* function $\chi_v(\mathbf{r})$ is an equivalent expression of the two-point correlation function $S_2^{(i)}(\mathbf{r})$ defined by $\chi_v(\mathbf{r}) \equiv S_2^{(1)}(\mathbf{r}) - \phi_1^2 = S_2^{(2)}(\mathbf{r}) - \phi_2^2$. The nonnegative *spectral density* $\tilde{\chi}_v(\mathbf{k})$, which can be obtained from scattering experiments [80,81], is the Fourier transform of $\chi_v(\mathbf{r})$ at wave vector $\mathbf{k}$, i.e., $\tilde{\chi}_v(\mathbf{k}) = \int_{\mathbb{R}^d} \chi_v(\mathbf{r}) e^{-i\mathbf{k}\cdot\mathbf{r}} d\mathbf{r} \geqslant 0$. Without loss of generality, we can always define the isotropic radial functions $\chi_v(r)$ and $\tilde{\chi}_v(k)$ by averaging the vector-dependent $\chi_v(\mathbf{r})$ and $\tilde{\chi}_v(\mathbf{k})$ over all angles, i.e., $\chi_v(r) = \frac{1}{\Omega}\int_\Omega \chi_v(\mathbf{r}) d\Omega$, $\tilde{\chi}_v(k) = \frac{1}{\Omega}\int_\Omega \tilde{\chi}_v(\mathbf{k}) d\Omega$ [17].

B. Classification of hyperuniform and nonhyperuniform media

For two-phase heterogeneous media in d-dimensional Euclidean space $\mathbb{R}^d$, *hyperuniformity* is defined by the following infinite-wavelength condition on the spectral density $\tilde{\chi}_v(\mathbf{k})$ [21,22], i.e., $\lim_{|\mathbf{k}|\to 0} \tilde{\chi}_v(\mathbf{k}) = 0$, which corresponds to $\alpha > 0$. Hyperuniformity generalizes the traditional notion of long-range order in many-particle systems to not only include all perfect crystals and perfect quasicrystals, but also exotic amorphous states of matter [20,22].

The hyperuniformity concept has led to a unified means of classifying equilibrium and nonequilibrium states of matter, whether hyperuniform or not, according to their large-scale fluctuation characteristics [17,19]. The hyperuniform two-phase media [21,22] are further divided into three different scaling regimes (classes) based on the associated large-R behaviors of the volume-fraction variance determined by the value of the scaling exponent α:

$$\sigma_v^2(R) \sim \begin{cases} R^{-(d+1)}, & \alpha > 1 \quad \text{(Class I)} \\ R^{-(d+1)} \ln R, & \alpha = 1 \quad \text{(Class II)} \\ R^{-(d+\alpha)}, & 0 < \alpha < 1 \quad \text{(Class III).} \end{cases} \tag{5}$$

Classes I and III are the strongest and weakest forms of hyperuniformity, respectively. Class I media with $\alpha \to \infty$, such as crystals, are known to be stealthy hyperuniform for possessing zero-scattering intensity for a set of wave vectors around the origin [82], i.e.,

$$\tilde{\chi}_v(\mathbf{k}) = 0 \quad \text{for } 0 \leqslant |\mathbf{k}| \leqslant K. \tag{6}$$

By contrast, for any nonhyperuniform two-phase system, the local variance has the following large-R scaling behaviors [30]:

$$\sigma_v^2(R) \sim \begin{cases} R^{-d}, & \alpha = 0 \,\text{(typical nonhyperuniform)} \\ R^{-(d+\alpha)}, & -d < \alpha < 0 \ \text{(antihyperuniform).} \end{cases} \tag{7}$$

For a "typical" nonhyperuniform system, $\tilde{\chi}_v(0) = B > 0$ is positive and bounded [22]. In antihyperuniform systems, $\lim_{|\mathbf{k}|\to 0} \tilde{\chi}_v(\mathbf{k}) = +\infty$ is unbounded [30], and hence are diametrically opposed to hyperuniform systems. Prototypical examples of "typical" nonhyperuniform and antihyperuniform systems involve equilibrium hard spheres and systems at thermal critical points (e.g., liquid-vapor and magnetic critical points) [83,84], respectively. The "phase diagram" with respect to the exponent α in Fig. 1 summarizes this classification.

C. Long-time asymptotic expansion of $\mathcal{I}^{\rm ex}(t)$

Suppose all of the moments $M_n(\chi_v) = \int_0^\infty r^n \chi_v(r) dr$ exist, Torquato [17] showed that $\mathcal{I}^{\rm ex}(t)$ can be expanded as

$$\begin{aligned} \mathcal{I}^{\rm ex}(t) &= \frac{d\omega_d}{(4\pi Dt)^{d/2}} \sum_{i=0}^{\infty} \frac{(-1)^i}{i!} \frac{M_{d-1+2i}(\chi_v)}{\phi_1\phi_2(4Dt)^i} \\ &= (Dt/a^2)^{-\frac{d+\alpha}{2}} \sum_{i=0}^{\infty} C_i (Dt/a^2)^{-i}, \end{aligned} \tag{8}$$

where $\alpha = 0, 2, 4, ...,$ and $\omega_d = \frac{\pi^{d/2}}{\Gamma(1+d/2)}$ is the volume of a d-dimensional sphere of unit radius. On the other hand, suppose the spectral density can be expanded as $\tilde{\chi}_v(k) = (ka)^\alpha [B + B_{\beta_1/2}(ka)^{\beta_1} + B_{\beta_2/2}(ka)^{\beta_2} + ...]$, then $\mathcal{I}^{\rm ex}(t)$ should be expanded as

$$\mathcal{I}^{\rm ex}(t) = (Dt/a^2)^{-\frac{d+\alpha}{2}} \sum_{i=0}^{\infty} C_{\beta_i/2} (Dt/a^2)^{-\beta_i/2}, \tag{9}$$

with

$$C_{\beta_i/2} = \frac{d\omega_d}{(2\pi)^d} \frac{B_{\beta_i/2}\Gamma[(d+\alpha+\beta_i)/2]}{2\phi_1\phi_2}. \tag{10}$$

Clearly, the asymptotic expansion of $\mathscr{I}^{\rm ex}(t)$ obtained from either the real-space or Fourier-space expansion must agree with each other; however, the Fourier-space expansion (9) apparently takes a more general form than the real-space expansion (8). In other words, if all of the moments $M_l(\chi_v)$ exist, then $\tilde{\chi}_v(k)$ is an analytic function at the origin [17], and vice versa. By contrast, if $\tilde{\chi}_v(k)$ is nonanalytic at the origin, some of the moments $M_l(\chi_v)$ are bound to diverge, and vice versa. The large-r behavior of $\chi_v(r)$, or equivalently, the analyticity of $\tilde{\chi}_v(k)$ at the origin, is thus encoded in the large-t asymptotic expansion of $\mathscr{I}^{\rm ex}(t)$.

Note that the long-time asymptotic expansion (8) or (9) may be convergent or divergent. For any fixed time t, the expansion (8) is convergent in the $n\to\infty$ limit only when $\lim_{n\to\infty}|(C_{n+1}t^{-n-1})/(C_nt^{-n})|<1$, i.e., $t>\lim_{n\to\infty}|C_{n+1}/C_n|$, and divergent if $\lim_{n\to\infty}|C_{n+1}/C_n|=\infty$. However, even if the series is divergent, the n-th-order truncated asymptotic expansion $\sum_{j=0}^{n}C_j(Dt/a^2)^{-\frac{d+\alpha}{2}-j}$ still approximates well the exact $\mathscr{I}^{\rm ex}(t)$ for some sufficiently long time, i.e., $\mathscr{I}^{\rm ex}(t)-\sum_{j=0}^{n}C_j(Dt/a^2)^{-\frac{d+\alpha}{2}-j}=O(t^{-\frac{d+\alpha}{2}-n-1}), t\to\infty$. The accuracy of the truncated series can be improved by increasing the order n for either the convergent series or the divergent series. For the latter instance, the improvement is optimized at a certain order $n_p(t)$, depending on the time t.

In the stealthy hyperuniform case where $\alpha\to\infty$, the predicted infinitely fast inverse-power decay rate implies that the infinite-time asymptote is approached exponentially fast [17]. For periodic media, the long-time excess spreadability scales as $\mathscr{I}^{\rm ex}(t)\sim Ce^{-K^2Dt}$; for disordered stealthy hyperuniform media, the long-time excess spreadability scales as $\mathscr{I}^{\rm ex}(t)\sim C\frac{\exp(-K^2Dt)}{K^2Dt}$.

D. Nonanalytic spectral density and irregular spreadability expansion

Consider a system of identical impenetrable particles of radius R in a matrix interacting via a pair potential $v(\mathbf{r})$ that scales as $v(\mathbf{r})\sim E/|\mathbf{r}|^{d+\zeta}, |\mathbf{r}|\to\infty$ for a constant E and $\zeta>0$. The effective potential between the centroids is $v_{\rm eff}(\mathbf{r})=v(\mathbf{r})+u(\mathbf{r})$, where $u(\mathbf{r})=\infty$ for $|\mathbf{r}|<R$ and $u(\mathbf{r})=0$ otherwise is the hard-core potential, which does not affect the large-distance scaling $v_{\rm eff}(\mathbf{r})\sim v(\mathbf{r})\sim E/|\mathbf{r}|^{d+\zeta}$. Torquato and Wang [85] show that for odd integer ζ, the *structure factor*[1] $S(\mathbf{k})$ associated with the positions of particle centers of the equilibrium system away from the critical point is given by

$$S(\mathbf{k})\sim-\frac{E}{k_BT}c_1(\zeta,d)\rho S(\mathbf{0})^2|\mathbf{k}|^{\zeta}+f(\mathbf{k}),\quad |\mathbf{k}|\to 0, \tag{11}$$

where $c_1(\zeta,d)$ is a function of ζ and dimension d, and $f(\mathbf{k})$ is an analytic function of $\mathbf{k}$ at the origin. As for even integer ζ, the expansion contains not just the $|\mathbf{k}|^{\zeta}$ term but also a $|\mathbf{k}|^{\zeta}\ln|\mathbf{k}|$ term [85]. The corresponding spectral density $\tilde{\chi}_v(\mathbf{k})$ when such a packing is mapped to a two-phase medium (identical impenetrable spheres in a matrix) is directly related to the structure factor $S(\mathbf{k})$ by [22]

$$\tilde{\chi}_v(\mathbf{k})=\phi_2\tilde{\alpha}_2(k;R)S(\mathbf{k}), \tag{12}$$

where ϕ_2 is the volume fraction of the spheres, and $\tilde{\alpha}_2(k;R)=\Gamma(d/2+1)k^{-d}J_{d/2}^2(kR)$ is the Fourier transform of the scaled intersection volume of two spherical windows. $\tilde{\alpha}_2(k;R)$ is analytic at the origin, so the $|\mathbf{k}|^{\zeta}$ and $|\mathbf{k}|^{\zeta}\ln|\mathbf{k}|$ singularity in $S(\mathbf{k})$ is preserved in the spectral density $\tilde{\chi}_v(\mathbf{k})$, which then enters the asymptotic expansion of $\mathscr{I}^{\rm ex}(t)$ via Eq. (9).

For instance, the Lennard-Jones potential $v_{\rm LJ}(\mathbf{r})=4\varepsilon[(\sigma/r)^{12}-(\sigma/r)^6]$ scales as $v_{\rm LJ}(\mathbf{r})\sim-4\varepsilon(\sigma/r)^6, r\to\infty$, i.e., $E=-4\varepsilon\sigma^6$ and $\zeta=3$ for $d=3$. Its structure factor near the origin can be expanded as

$$S(\mathbf{k})=s_0+s_2|\mathbf{k}|^2+4\rho\beta\varepsilon\sigma^6c_1(3,3)s_0^2|\mathbf{k}|^3+s_4|\mathbf{k}|^4+..., \tag{13}$$

which contains no first-order term but a third-order term, a signature of the $\zeta=3$ interaction and correlation in the system. Correspondingly, the asymptotic expansion of the spectral density also contains a singular $|\mathbf{k}|^3$ term, i.e.,

$$\tilde{\chi}_v(\mathbf{k})=B_0+B_1|\mathbf{k}\sigma|^2+B_{3/2}|\mathbf{k}\sigma|^3+B_2|\mathbf{k}\sigma|^4+..., \tag{14}$$

which results in an irregular spreadability expansion in contrast to the regular expansion (8):

$$\mathscr{I}^{\rm ex}(t)=t^{-3/2}[C_0+C_1(Dt/\sigma^2)^{-1}+C_{3/2}(Dt/\sigma^2)^{-3/2}+C_2(Dt/\sigma^2)^{-2}+...]. \tag{15}$$

III. THEORY OF LONG-TIME SPREADABILITY ASYMPTOTIC EXPANSION

A. Classification of the long-time spreadability asymptotics

In this subsection, we provide a unified classification of the basic asymptotic behaviors of the long-time normalized excess spreadability $\mathscr{I}^{\rm ex}(t)$ under certain conditions, e.g., hyperuniform or nonhyperuniform media, media with spectral densities analytic or nonanalytic at the origin, and media with or without long-range orders. Some of the results have already been reported in previous works [17,85]. For clarity and simplicity, we henceforth set both the diffusion coefficient D and the characteristic heterogeneity length scale a to be unity, i.e., $D=a=1$, without loss of generality.

For disordered two-phase media without any long-range order, the spectral density $\tilde{\chi}_v(k)$ contains no Bragg peaks. If $\tilde{\chi}_v(k)$ is analytic at the origin so that its expansion contains only regular powers $1, k^2, k^4, ...$, the autocovariance function $\chi_v(r)$ decays faster than any power law at large distance r so that all of the moments $M_n(\chi_v)$ exist, and the regular expansion (8) applies. On the other hand, the singular powers $k^{\zeta}, \zeta\neq 0, 2, 4...$ and the generalized powers $k^{\zeta}\ln k, \zeta=0, 2, 4...$ are proportional to the Fourier transform of $r^{-d-\zeta}$ [85,87,88]. More detailed information about the Fourier transform of the power law is presented in Appendix A.

There are some exceptions when the spectral density $\tilde{\chi}_v(k)$ cannot be expanded in terms of powers at the origin: stealthy hyperuniform media with $\tilde{\chi}_v(k)\equiv 0$ near the origin, periodic media with discontinuous $\tilde{\chi}_v(k)$ due to the Bragg peaks [19], as well as quasicrystals with dense Bragg peaks [79]. For quasicrystals, the long-time spreadability $\mathscr{I}^{\rm ex}(t)$ oscillates between two asymptotic power laws of the same exponent α

[1]The structure factor is defined by the Fourier transform of the pair correlation function [22,86].

TABLE I. Classification of two-phase media and the corresponding long-time normalized excess spreadability $\mathcal{I}^{\rm ex}(t)$ behaviors. We only list the leading order terms, but the general form of the expansion can be inferred from the linear combination of these terms due to the linearity of Eq. (1). Both the diffusion coefficient D and the characteristic heterogeneity length scale a are set to be unity, i.e., $D = a = 1$.

Leading term in long-time Asymptotic expansion of spreadability ($\gamma \equiv \frac{d+\alpha}{2}, D = a = 1, t \to \infty$)			Disordered		Ordered	
			Regular ($\alpha/2 \in \mathbb{N}$)	Singular ($\alpha = \zeta$)	Crystal	Quasicrystal
Hyperuniform ($\alpha > 0$)	Class I ($\alpha > 1$)	Stealthy hyperuniform ($\alpha \to \infty$)	$C\frac{e^{-K^2t}}{K^2t}$		Ce^{-K^2t}	
		Nonstealthy hyperuniform ($0 < \alpha < \infty$)	$Ct^{-\gamma}$	$Ct^{-\gamma}$ (if $\alpha/2 \notin \mathbb{N}_+$), $Ct^{-\gamma}\ln\frac{t}{t_0}$ (if $\alpha/2 \in \mathbb{N}_+$)		oscillate between $C_\pm t^{-\gamma}$
	ClassII ($\alpha = 1$)			$Ct^{-\gamma}$		oscillate between $C_\pm t^{-\gamma}$
	Class III ($0 < \alpha < 1$)			$Ct^{-\gamma}$		
Nonhyperuniform ($-d < \alpha \leqslant 0$)	Typical nonhyperuniform ($\alpha = 0$)		$Ct^{-\gamma}$	$Ct^{-\gamma}\ln\frac{t}{t_0}$		
	Antihyperuniform ($-d < \alpha < 0$)			$Ct^{-\gamma}$		

but different coefficients $C_\pm$. This completes our classification of the long-time asymptotic behaviors of $\mathcal{I}^{\rm ex}(t)$ of all known kinds of two-phase media as summarized in Table I. The general form of the asymptotic expansion series can be inferred from Table I based on the linearity of Eq. (1).

By incorporating correction terms in the asymptotic expansion to the fitting function, we can extract information from the long-time $\mathcal{I}^{\rm ex}(t)$ data much more accurately and efficiently, which is the main focus of Secs. IV and V. In the next subsection, we extend our long-time spreadability analysis to other times to obtain accurate approximants of $\mathcal{I}^{\rm ex}(t)$ for all times.

B. Approximants of the spreadability for all times

The long-time asymptotic expansion of the spreadability $\mathcal{I}^{\rm ex}(t) = t^{-\frac{d+\alpha}{2}}\sum_{i=0}^{\infty} C_{\beta_i/2}t^{-\beta_i/2}$, together with its short-time counterpart $\mathcal{I}^{\rm ex}(t) = \sum_{j=0}^{\infty} A_j t^{j/2}$, allow us to construct accurate approximants for all times. The most straightforward approximants are the one-point polynomials $P_\infty^{(n)}(t)$ and $P_0^{(n)}(t)$, defined as simple truncations of the long- and short-time expansions of $\mathcal{I}^{\rm ex}(t)$ at the order n, i.e.,

$$P_\infty^{(n)}(t) = t^{-\frac{d+\alpha}{2}}\sum_{i=0}^{n} C_{\beta_i/2}t^{-\beta_i/2} \quad \text{(long times)}, \tag{16}$$

$$P_0^{(n)}(t) = \sum_{j=0}^{n} A_j t^{j/2} \quad \text{(short times)}, \tag{17}$$

where the coefficient $A_0 \equiv 1$, since $P_0^{(n)}(0) = \mathcal{I}^{\rm ex}(0) \equiv 1$. Clearly, $P_\infty^{(n)}(t)$ approximates $\mathcal{I}^{\rm ex}(t)$ well at long times, while $P_0^{(n)}(t)$ approximates $\mathcal{I}^{\rm ex}(t)$ well at short times. Note that neither of the polynomials is very accurate at intermediate times. Particularly, the asymptotic expansion may sometimes be divergent, causing the deviation of $P_\infty^{(n)}(t)$ or $P_0^{(n)}(t)$ to grow rather than diminish with the order n after the order exceeds an optimal order $n_p(t)$ at time t.

One well-known way to improve the accuracy of the polynomial approximants is to use them to form Padé approximants [89], i.e., rational functions. Specifically, the one-point Padé approximants $R_\infty^{(n)}(t)$ and $R_0^{(n)}(t)$ are given as

$$R_\infty^{(n)}(t) = t^{-\frac{d+\alpha}{2}}\mathcal{R}_{t\to\infty}[C_{\beta_i/2}t^{-\beta_i/2}] \quad \text{(long times)}, \tag{18}$$

$$R_0^{(n)}(t) = \mathcal{R}_{t=0}\left[\sum_{j=0}^{n} A_j t^{j/2}\right] \quad \text{(short times)}, \tag{19}$$

where $\mathcal{R}_{x=x_0}[p(x)]$ denotes the operation of converting the polynomial $p(x)$ into a Padé expression around $x = x_0$. More details about the Padé approximants are presented in Appendix B. The key conclusion is that the one-point Padé approximants $R_\infty^{(n)}(t)$ and $R_0^{(n)}(t)$ can present much better approximation for the intermediate-time behaviors of $\mathcal{I}^{\rm ex}(t)$ while maintaining the correct long-/short-time behaviors, respectively.

Importantly, we can approximate $\mathcal{I}^{\rm ex}(t)$ for all times by combining the long-time Padé approximant $R_\infty^{(n)}(t)$ and the short-time Padé approximant $R_0^{(n)}(t)$ into the following two-point Padé approximant:

$$R_{0;\infty}^{(m,n)}(t) = \frac{R_0^{(m)}(t)}{1+(t/t_0)^\nu} + \frac{R_\infty^{(n)}(t)}{1+(t/t_0)^{-\nu}}, \quad \nu > \frac{d+\alpha+m+\beta_n}{2}. \tag{20}$$

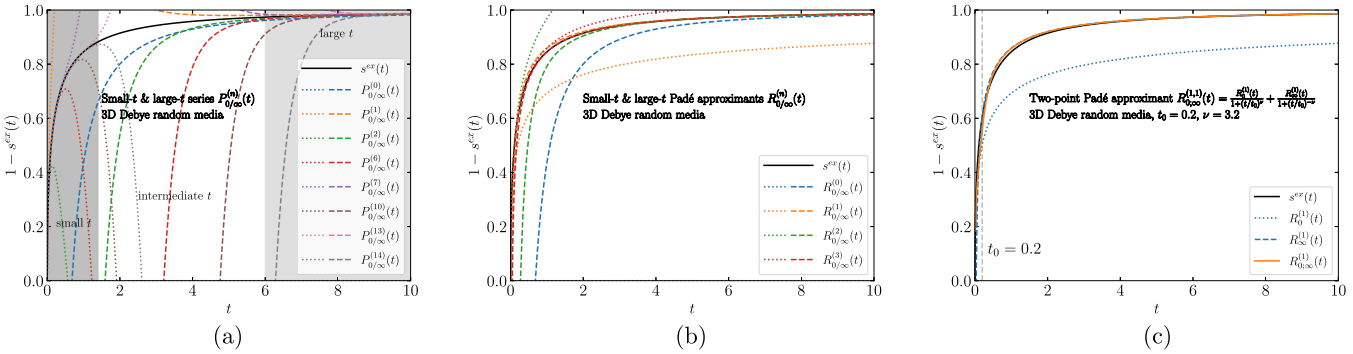


FIG. 2. (a) The numerical results of the truncated series $P_0^{(n)}(t)$ and $P_\infty^{(n)}(t)$ [Eqs. (17) and (16)] against the exact $\mathcal{I}^{\rm ex}(t)$. The small-, intermediate-, and large-t regions distinguished by different shadows are settled semi-quantitatively based on the agreement between $P_0^{(n)}(t)$, $P_\infty^{(n)}(t)$, and $\mathcal{I}^{\rm ex}(t)$. (b) Padé approximants $R_0^{(n)}(t)$ and $R_\infty^{(n)}(t)$ [Eqs. (19) and (18)] in contrast to the exact $\mathcal{I}^{\rm ex}(t)$. (c) The two-point Padé approximant $R_{0;\infty}^{(1,1)}(t)$ [Eq. (20)] that resumes the correct short- and large-t behaviors up to the same order as $R_0^{(1)}(t)$ and $R_\infty^{(1)}(t)$. In all three plots, (a)–(c), both the diffusion coefficient D and the characteristic heterogeneity length scale a are set to be unity, i.e., $D = a = 1$.

Similarly, one can further improve these estimates in the intermediate-time region by incorporating intermediate-time terms to get a three-point Padé approximant. In this way, we can approximate $\mathcal{I}^{\rm ex}(t)$ with just a few parameters while constraining it to match the most important short-, intermediate-, and long-time features. Our parametrization scheme of the spreadability can improve the efficiency of time-dependent diffusive transport property engineering [90]. Specifically, it can be useful in the inverse design of self-assembly patterns that manifest desired spreadability properties.

Figure 2 contrasts the one-point polynomials $P_\infty^{(n)}(t)$ and $P_0^{(n)}(t)$, the corresponding one-point Padé approximants $R_\infty^{(n)}(t)$ and $R_0^{(n)}(t)$, as well as the two-point Padé approximant $R_{0;\infty}^{(1,1)}(t)$ for Debye random media (DRM). (Additional information about this specific example model can be found in Appendix C 1.) Not surprisingly, due to the divergent nature of $P_\infty^{(n)}(t)$ for DRM, its deviation from the exact $\mathcal{I}^{\rm ex}(t)$ decreases at first but eventually grows with the order n at any fixed t in Fig. 2(a), limiting its accuracy as an approximant, especially at the short and intermediate time range. This divergence effect of $P_\infty^{(n)}(t)$ is demonstrated more explicitly in Fig. 3, where we explicitly show the decrease and increase of its deviation from the exact $\mathcal{I}^{\rm ex}(t)$. Despite being a convergent series, $P_0^{(n)}(t)$ converges rather slowly and also deviates drastically from $\mathcal{I}^{\rm ex}(t)$ at the intermediate times, not to mention the long-time region. By contrast, the corresponding Padé expression $R_\infty^{(n)}(t)$ exhibits superior convergence and accuracy in Fig. 2(b), especially at the intermediate-time region. Finally and importantly, the two-point Padé approximant $R^{(1,1)}(t)$ in Fig. 2(c) provides an excellent approximation of the exact $\mathcal{I}^{\rm ex}(t)$ at any time t, despite involving only three independent coefficients A_1, C_0, and C_1 ($A_0 \equiv 1$).

IV. LONG-TIME ASYMPTOTIC FITTING SCHEME

Given the lessons learned about getting accurate approximations of the asymptotic behavior of $\mathcal{I}^{\rm ex}(t)$ (Sec. III), we now proceed to estimating such long-time behaviors when $\mathcal{I}^{\rm ex}(t)$ is extracted from numerical or experimental data, which often occurs in practice. The ensuing fitting procedure applies to the restricted class of microstructure described by long-time spread that involves the power law, i.e, nonhyperuniform as well as nonstealthy hyperuniform disordered microstructure described in Table I. Clearly, such estimates require fitting the spreadability data at sufficiently long times. All such previous works [19,79] estimate the exponent α in the asymptotic power law $\mathcal{I}^{\rm ex}(t) \sim Ct^{-\frac{d+\alpha}{2}}$, $t \to \infty$ by taking the logarithm of both sides to get

$$\ln\left[\hat{\mathcal{I}}_0^{\rm ex}(t)\right] = \ln \hat{C} - \frac{d+\hat{\alpha}}{2} \ln t, \tag{21}$$

and then fitting this form at sufficiently large times t using a standard least-squares regression, i.e., minimizing the sum of $(\ln[\mathcal{I}^{\rm ex}(t)] - \ln[\hat{\mathcal{I}}_0^{\rm ex}(t)])^2$ for all data points. We use the hat symbol above quantities to distinguish the fitting function and fitting parameters from the raw data and fixed parameters. In what follows, we propose three types of fitting functions by incorporating correction terms to the original fitting function $\ln[\hat{\mathcal{I}}_0^{\rm ex}(t)]$.

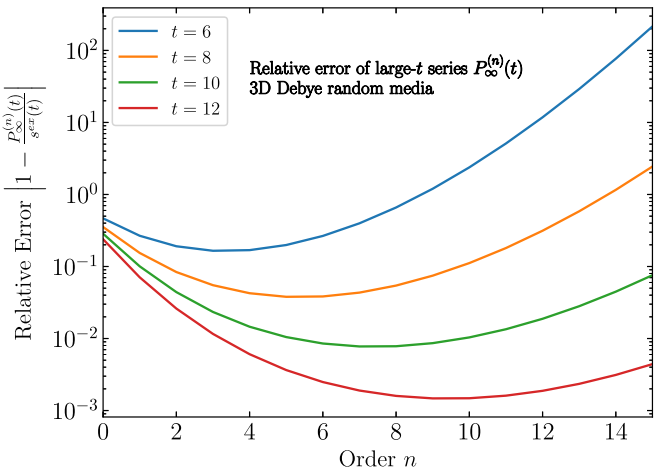


FIG. 3. The relative error of the truncated long-time asymptotic expansion $P_\infty^{(n)}(t)$ [Eq. (16)] against the exact $\mathcal{I}^{\rm ex}(t)$ of different order n at different times t. Both the diffusion coefficient D and the characteristic heterogeneity length scale a are set to be unity, i.e., $D = a = 1$.

A. Three types of improved fitting functions

We intend to improve the fitting function $\ln[\hat{\mathcal{I}}_0^{\rm ex}(t)]$ by incorporating correction terms in the long-time asymptotic expansion of $\mathcal{I}^{\rm ex}(t)$. However, the most general form (9) of the asymptotic expansion is unstable as a fitting function if all the exponents α and β_i are set to be free fitting parameters. In order to strike a balance between the generality of the fitting procedure and numerical stability, we propose three types of fitting functions by adding three different types of corrections to the fitting function $\ln[\hat{\mathcal{I}}_0^{\rm ex}(t)]$ based on different assumptions about the exponents α and β_i.

(1) *Type I*. Assume that $\beta_i = i = 1, 2, 3, ...$, and thus the spectral density expansion takes the form

$$\tilde{\chi}_v(k) = k^\alpha(B + B_{1/2}k + B_1k^2 + ...), \tag{22}$$

which, if α is not an integer, corresponds to an autocovariance function of the form

$$\chi_v(r) = r^{-d-\alpha}(K + K_{1/2}r^{-1} + K_1r^{-2} + ...). \tag{23}$$

The corresponding spreadability asymptotic expansion is given by $\mathcal{I}^{\rm ex}(t) = t^{-\frac{d+\alpha}{2}}(C + C_{1/2}t^{-1/2} + C_1t^{-1} + ...)$, and so we have the first type of fitting function

$$\ln\left[\hat{\mathcal{I}}_1^{\rm ex}(t)\right] = -\frac{d+\hat{\alpha}}{2}\ln t + \ln\left(\sum_{i=0}^{n}\hat{C}_{i/2}t^{-i/2}\right). \tag{24}$$

When $n = 0$, $\ln[\hat{\mathcal{I}}_1^{\rm ex}(t)]$ reduces to the original fitting function $\ln[\hat{\mathcal{I}}_0^{\rm ex}(t)]$ [Eq. (21)]. We can improve the fitting by considering $n \geqslant 1$.

(2) *Type II*. Still assuming that $\beta_i = i = 1, 2, 3, ...$, if α takes an integer value, the Fourier transform of the same autocovariance function form

$$\chi_v(r) = r^{-d-\alpha}(K + K_{1/2}r^{-1} + K_1r^{-2} + ...), \tag{25}$$

involves generalized power-law terms like $\ln k$, $k^2\ln k$, $k^4\ln k$, ..., which shall thus be taken into account in the spectral density expansion, i.e.,

$$\tilde{\chi}_v(k) = k^\alpha\sum_{i=0}^{\infty}B_{i/2}k^i + k^{2\lceil\alpha/2\rceil_+}\ln k\sum_{j=0}^{\infty}F_jk^{2j}, \tag{26}$$

where $\alpha \in \mathbb{Z}$. Correspondingly, the spreadability asymptotic expansion is given by

$$\mathcal{I}^{\rm ex}(t) = t^{-\frac{d+\alpha}{2}}\sum_{i=0}^{\infty}C_{i/2}t^{-i/2} + t^{-d/2-\lceil\alpha/2\rceil_+}\ln t\sum_{j=0}^{\infty}E_jt^{-j}. \tag{27}$$

TABLE II. The expressions of the three types of fitting functions, where $\hat{\alpha}$ and $\hat{C}_{\beta_i/2}$ denote the fitting parameters to be determined from the fitting, n is the fitting order, while t, d, α, $\Delta = \lceil\alpha/2\rceil_+ - \alpha/2$, and $m = \lfloor(\alpha+n)/2\rfloor - \lceil\alpha/2\rceil_+$ are fixed parameters set to be the input of the fitting.

The three types of fitting functions	
Type I	$\ln[\hat{\mathcal{I}}_1^{\rm ex}(t)] = -\frac{d+\hat{\alpha}}{2}\ln t + \ln(\sum_{i=0}^{n}\hat{C}_{i/2}t^{-i/2})$
Type II	$\ln\left[\hat{\mathcal{I}}_2^{\rm ex}(t)\right] = -\frac{d+\alpha}{2}\ln t + \ln\left(\sum_{i=0}^{n}\hat{C}_{i/2}t^{-i/2} + t^{-\Delta}\ln t\sum_{j=0}^{m}\hat{E}_jt^{-j}\right)$
Type III	$\ln\left[\hat{\mathcal{I}}_3^{\rm ex}(t)\right] = -\frac{d+\alpha}{2}\ln t + \ln\left(\sum_{i=0}^{n}\hat{C}_it^{-i}\right)$

The second type of fitting function is then given by

$$\ln\left[\hat{\mathcal{I}}_2^{\rm ex}(t)\right] = -\frac{d+\alpha}{2}\ln t + \ln\left(\sum_{i=0}^{n}\hat{C}_{i/2}t^{-i/2} + t^{-\Delta}\ln t\sum_{j=0}^{m}\hat{E}_jt^{-j}\right), \tag{28}$$

where $\Delta = \lceil\alpha/2\rceil_+ - \alpha/2$ and $m = \lfloor(\alpha+n)/2\rfloor - \lceil\alpha/2\rceil_+$. The integer α assumption eliminates the possibility of Class III hyperuniform media.

(3) *Type III*. If we assume $\beta_i = 2i = 2, 4, 6, ...$, meaning that the spectral density is analytic at the origin, i.e.,

$$\tilde{\chi}_v(k) = k^\alpha(B + B_1k^2 + B_2k^4 + ...), \quad \alpha/2 \in \mathbb{N}, \tag{29}$$

then the autocovariance function $\chi_v(r)$ decays faster than any power law at large distance r so that all of the moments $M_n(\chi_v)$ exist, and the regular expansion (8) applies, i.e., $\mathcal{I}^{\rm ex}(t) = t^{-\frac{d+\alpha}{2}}(C + C_1t^{-1} + C_2t^{-2} + ...)$. Thus, the third type of fitting function takes the form

$$\ln\left[\hat{\mathcal{I}}_3^{\rm ex}(t)\right] = -\frac{d+\alpha}{2}\ln t + \ln\left(\sum_{i=0}^{n}\hat{C}_it^{-i}\right), \tag{30}$$

where $\alpha/2 \in \mathbb{N}$. The non-negative even integer α assumption narrows the possibilities down to typical nonhyperuniform and Class I hyperuniform media.

For convenience, we summarize the three types of fitting functions in Table II and the classes of microstructures to which they apply in Table III.

B. Fitting procedure

In practice, we often have no prior knowledge about the functional form of the expansion of the spectral density $\tilde{\chi}_v(k)$ of the heterogeneous medium of interest. In those cases, we propose the following systematic procedure:

(1) Fit with Type I $\ln[\hat{\mathcal{I}}_1^{\rm ex}(t)]$ (24) first, which makes the weakest assumption and thus applies to the broadest range of media among the three.

(2) According to the fitting results $\hat{\alpha}$ and $\hat{C}_i$ of $\ln[\hat{\mathcal{I}}_1^{\rm ex}(t)]$, attempt to fit with Type II or III if one of the following criteria is met:

(a) fit with Type II $\ln[\hat{\mathcal{I}}_2^{\rm ex}(t)]$ (28) if $|\hat{\alpha} - \alpha| \ll 1$ for an integer α.

TABLE III. Applicability of the three types of fitting functions for different two-phase media. Note that only a subset of the classification given by Table I is covered, namely, nonhyperuniform disordered media as well as hyperuniform disordered media that are not stealthy.

Classes of microstructures to which the fitting functions apply		Disordered	
		Regular ($\alpha/2 \in \mathbb{N}$)	Singular ($\alpha = \zeta$)
Nonstealthy hyperuniform ($0 < \alpha < \infty$)	Class I ($\alpha > 1$)	Type III	Types I and II
	Class II ($\alpha = 1$)		Type II
	Class III ($0 < \alpha < 1$)		Type I
Nonhyperuniform ($-d < \alpha \leqslant 0$)	Typical nonhyperuniform ($\alpha = 0$)	Type III	Type II
	Antihyperuniform ($-d < \alpha < 0$)		Types I and II

(b) fit with Type III $\ln[\hat{\mathcal{I}}_3^{\rm ex}(t)]$ (30) if $|\hat{\alpha} - \alpha| \ll 1$ for a non-negative even integer α and $|\hat{C}_{i/2}| \approx 0$ for odd i (Quantitatively, if $|\hat{C}_{1/2}| \ll \sqrt{|\hat{C}\hat{C}_1|}$, $|\hat{C}_{3/2}| \ll \sqrt{|\hat{C}_1\hat{C}_2|}$,...).

The fitting procedure is summarized in the following flow chart:

$$\mathcal{I}^{\rm ex}(t) \text{ data} \Rightarrow \text{Type I fitting} \Rightarrow \text{fitting results } \hat{\alpha}\&\hat{C}_{i/2}$$
$$\Rightarrow \begin{cases} \text{if } \hat{\alpha} \approx 0, 2, 4, \ldots \\ \&\hat{C}_{\frac{1}{2},\frac{3}{2},\ldots} \approx 0 & \rightarrow \text{switch to Type III fitting} \\ \text{else if } \hat{\alpha} \approx \text{integer} & \rightarrow \text{switch to Type II fitting} \\ \text{else} & \rightarrow \text{keep the Type I fitting} \end{cases}$$

For each of the three fitting functions we propose, the fitting order n determines the number of fitting parameters. Additional fitting parameters should be able to improve the accuracy of the fits; still, too many tend to lead to overfitting, i.e., the fitting accuracy degrades rather than improves by incorporating additional fitting parameters. Consequently, there should be an optimal fitting order n_o separating the underfitting and overfitting regions, which shall be settled by comparing the fits across different orders. In the underfitting region ($n < n_o$), as the order n increases to approach the optimal fitting order n_o, the fits should exhibit a converging trend, which stabilizes in the vicinity of the optimal order $n = n_o$. In the overfitting region ($n > n_o$), as the order n further increases, the fits demonstrate a (usually abruptly) different trend than in the underfitting region, or simply become unstable.

V. APPLICATIONS TO NONHYPERUNIFORM, HYPERUNIFORM, AND ANTIHYPERUNIFORM MEDIA

Here, we demonstrate the accuracy of our fitting procedure to ascertain the long-time asymptotic behaviors of the spreadability for three different models: (1) Debye random media, (2) hyperuniform media, and (3) antihyperuniform media. These models are purposely chosen because they span the possible range of large-scale structural properties of two-phase media. Debye random media are an example of typical nonhyperuniform media with $\alpha = 0$, the disordered hyperuniform model is Class I media with $\alpha = 2$ (possessing some vanishing coefficients ($C_{2i+1} = 0$ for 2D and $C_{3i+2} = 0$ for 3D), and the antihyperuniform model with $\alpha = -1$. We begin by generating exact (noise-free) discrete data sets of the spreadabilities for these models by substituting exact analytical forms for their two-point statistics, given in Appendix C, into Eq. (1). Such fits yield the highest possible accuracy that we can achieve with our fitting scheme. Then, we add Gaussian noise of varying magnitudes to the data to test its robustness to random noise in real data. In what follows, $\mathcal{I}^{\rm ex}(t)$

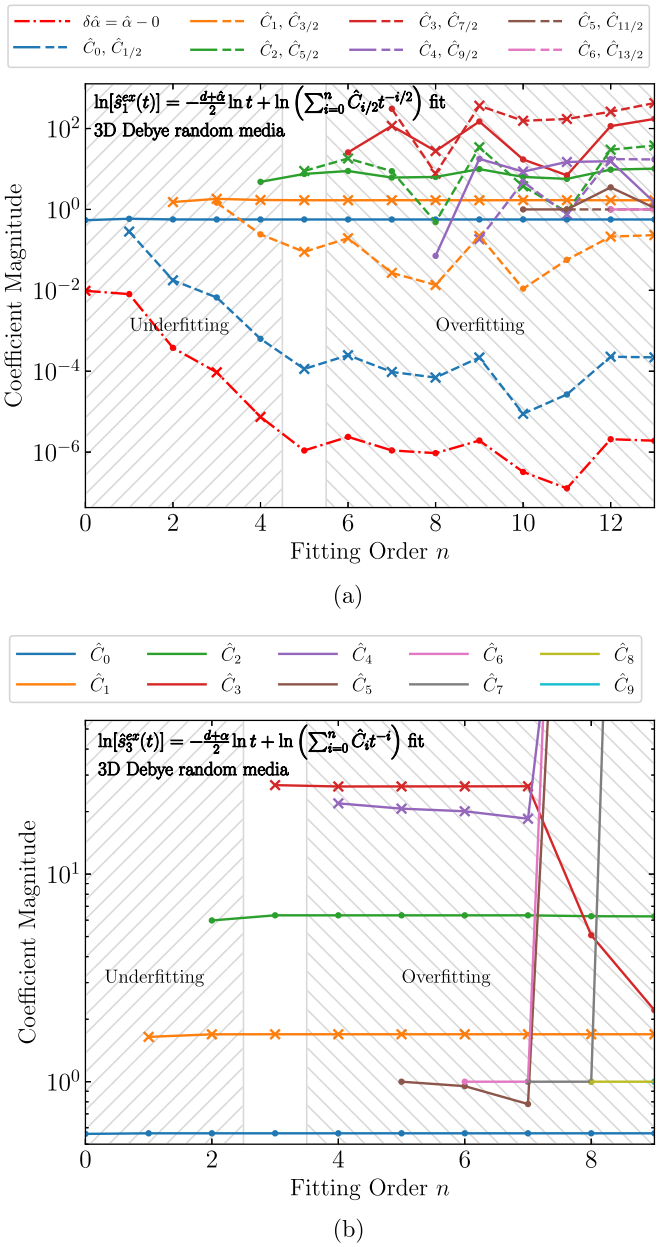


FIG. 4. Results of the fitting functions (a) $\ln[\hat{\mathcal{I}}_1^{\rm ex}(t)]$ [Eq. (24)] and (b) $\ln[\hat{\mathcal{I}}_3^{\rm ex}(t)]$ [Eq. (30)] for DRM spreadability [Eq. (C3)]. Positive and negative coefficients are indicated by filled circles and crosses, respectively. The underfitting region ($n < n_o$) and the overfitting region ($n > n_o$) are forward slash and backslash hatched, respectively, while the optimal fitting ($n = n_o$) is left blank.

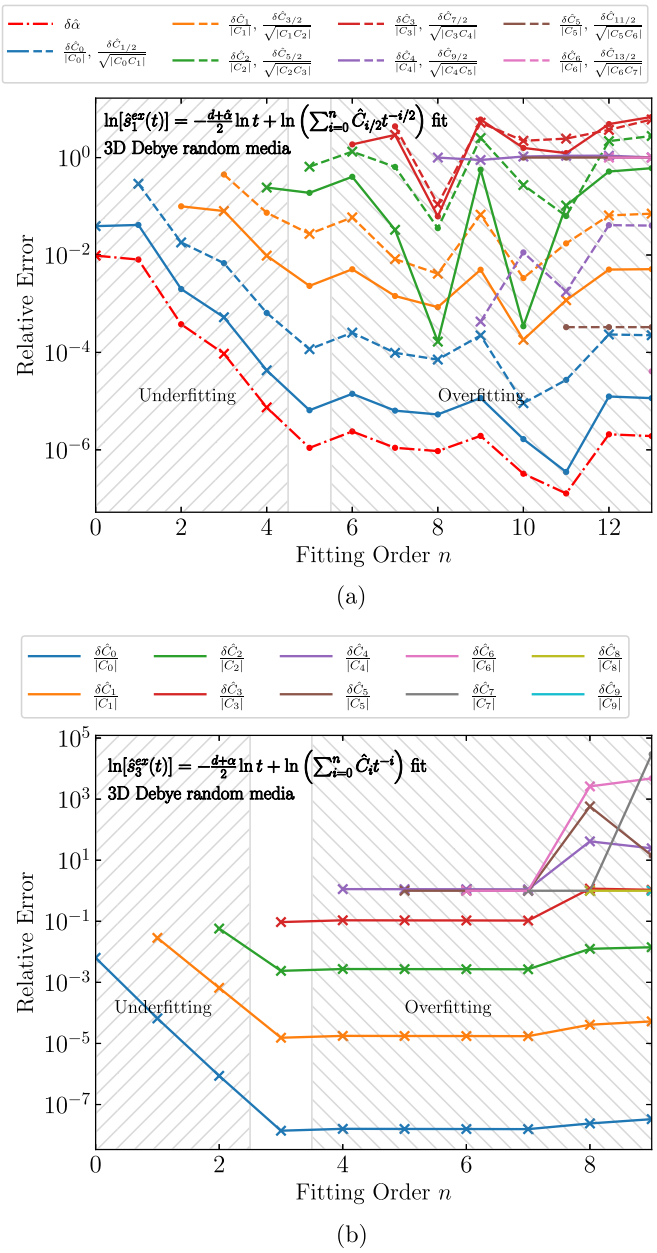


FIG. 5. Relative fitting errors of (a) $\ln[\hat{\jmath}_1^{\rm ex}(t)]$ [Eq. (24)] and (b) $\ln[\hat{\jmath}_3^{\rm ex}(t)]$ [Eq. (30)] compared to the exact values for Debye random media [Eq. (C3)]. Positive and negative relative errors are indicated by filled circles and crosses, respectively. The underfitting region ($n < n_o$) and the overfitting region ($n > n_o$) are forward slash and backslash hatched, respectively, while the optimal fitting ($n = n_o$) is left blank. The fit with $n = 0$ in **(a)** is equivalent to Wang and Torquato's fitting method proposed in [19].

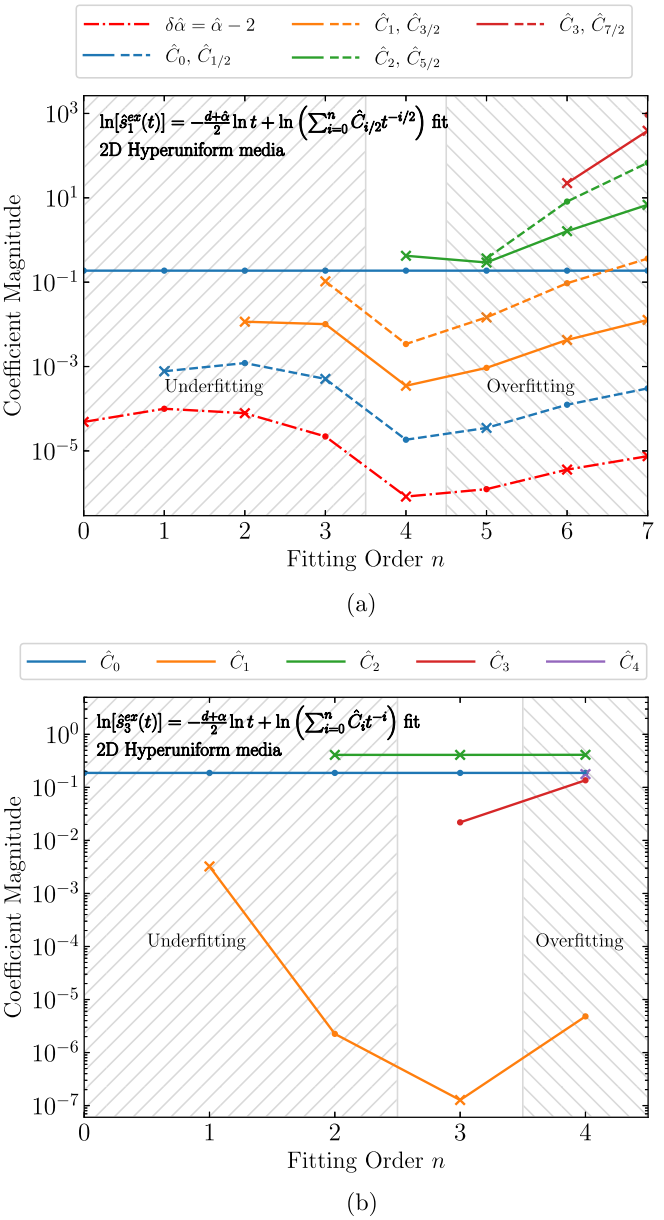


FIG. 6. (a) Type I [Eq. (24)] and (b) Type III [Eq. (30)] fits of $\mathfrak{z}^{\rm ex}(t)$ for 2D disordered hyperuniform media [Eq. (C9)]. Positive and negative coefficients are indicated by filled circles and crosses, respectively. The underfitting region ($n < n_o$) and the overfitting region ($n > n_o$) are forward slash and backslash hatched, respectively, while the optimal fitting ($n = n_o$) is left blank.

is computed for 1000 data points evenly distributed on the log scale from $t_{\rm min} = 100$ to $t_{\rm max} = 10000$, where, as noted earlier, we set both the diffusion coefficient D and the characteristic heterogeneity length scale a to be unity, i.e., $D = a = 1$.

A. Fitting with exact representations of $\mathfrak{z}^{\rm ex}(t)$

1. Debye random media

We first implement the Type I fitting procedure for Debye random media, and the results are shown in Fig. 4(a). As can be seen from the figure, $|\delta\hat{\alpha}| = |\hat{\alpha} - 0|$ continuously decreases down to $\sim 10^{-6}$ as the order n increases up to the optimal order $n_o = 5$ and keeps decreasing even in the overfitting region $n > n_o$, so one can conclude that $\alpha = 0$ within the error range. Also, the absolute values of half-integer-indexed coefficients (namely, $\hat{C}_{1/2}$ and $\hat{C}_{3/2}$ plotted in dashed lines) are systematically smaller than those of integer-indexed coefficients ($\hat{C}_0$, $\hat{C}_1$, and $\hat{C}_2$ plotted in solid lines); quantitatively, we can verify the dimensionless $|\hat{C}_{1/2}|/\sqrt{|\hat{C}_0\hat{C}_1|} \sim 10^{-4} \ll 1$ and $|\hat{C}_{3/2}|/\sqrt{|\hat{C}_1\hat{C}_2|} \sim 10^{-1} \ll 1$. We can thus conclude that $C_{1/2} = C_{3/2} = 0$ within the prescribed margin of error, and

then reasonably assume the analyticity of the spectral density at the origin.

Consequently, we then fit the same data with the Type III fitting function $\ln[\hat{\mathcal{I}}_3^{\rm ex}(t)]$, the results of which are shown in Fig. 4(b). As the fitting order n increases from 0 to $n_o = 3$, the fits steadily converge. Then the overfitting effect kicks in, and the fits become increasingly inaccurate. The final optimal fit ($n_o = 3$) is given by

$$\mathcal{I}^{\rm ex}(t) = t^{-\frac{d}{2}}(\hat{C} + \hat{C}_1 t^{-1} + \hat{C}_2 t^{-2} + \hat{C}_3 t^{-3}), \tag{31}$$

agreeing perfectly with the exact expansion (C3) truncated at the same order. In addition to the exponent $\alpha = 0$ and the coefficients $\hat{C}_i$, whose relative errors compared to the exact values are plotted in Fig. 5, this fit indicates the analyticity of the spectral density $\tilde{\chi}_V(k)$ at the origin up through $k^{\alpha+\beta_3} = k^6$, or equivalently, the existence of the moment $M_{d-1+6/2}(\chi_V) = M_5(\chi_V)$, i.e., $\chi_V(r) = o(r^{-6})$ as $r \to \infty$.

2. *Disordered hyperuniform media*

Figure 6(a) plots the results of the Type I fitting function $\ln[\hat{\mathcal{I}}_1^{\rm ex}(t)]$ for $d = 2$, where $|\delta\hat{\alpha}| = |\hat{\alpha} - 2|$ continuously decreases down to $\lesssim 10^{-5}$ as the order n increases up to the optimal order $n_o = 4$, implying $\alpha = 2$ within the error range. Notice that the magnitudes of $\hat{C}_{1/2}$, $\hat{C}_1$, and $\hat{C}_{3/2}$ are systematically much smaller than those of $\hat{C}_0$ and $\hat{C}_2$, and their signs constantly flip across different orders n in contrast to order coefficients, implying that $\hat{C}_{1/2} = \hat{C}_1 = \hat{C}_{3/2} = 0$ within the error range. We thus assume that the spectral density is analytic at the origin with $\alpha = 2$ and fit the $\mathcal{I}^{\rm ex}(t)$ data with the Type III fitting function $\ln[\hat{\mathcal{I}}_3^{\rm ex}(t)]$, the results of which are plotted in Fig. 6(b).

At the optimal fitting order $n_o = 3$, we have $|\hat{C}_1|/\sqrt{|\hat{C}_0\hat{C}_2|} \sim 10^{-6} \ll 1$, agreeing again with our assumption that $C_{1/2} = C_1 = C_{3/2} = 0$. The final optimal fit ($n_o = 3$) is given by

$$\mathcal{I}^{\rm ex}(t) = t^{-\frac{d+2}{2}}(\hat{C} + \hat{C}_1 t^{-1} + \hat{C}_2 t^{-2} + \hat{C}_3 t^{-3}), \tag{32}$$

where $|\hat{C}_1|/\sqrt{|\hat{C}_0\hat{C}_2|} \sim 10^{-6} \ll 1$ and $|\hat{C}_3|/\sqrt{|\hat{C}_2^3/\hat{C}_0|} \sim 10^{-1} < 1$, agreeing with the exact expansion at the same order

$$\mathcal{I}^{\rm ex}(t) = t^{-\frac{d+2}{2}}(C + C_2 t^{-2} + \ldots). \tag{33}$$

In addition to the exponent $\alpha = 2$ and the coefficients $\hat{C}_i$ themselves, we can infer that the spectral density $\tilde{\chi}_V(k)$ is analytic at the origin up to the order of $k^{\alpha+\beta_3} = k^8$. Equivalently, the moment $M_{d-1+8/2}(\chi_V) = M_5(\chi_V)$ exists, i.e., $\chi_V(r) = o(r^{-6})$ as $r \to \infty$. The inferences that $\alpha = 2$, $|\hat{C}_1| = 0$, and $|\hat{C}_3| \approx 0$ further imply that $M_{d-1}(\chi_V) = 0$, $M_{d+1}(\chi_V) = 0$, and $M_{d+3}(\chi_V) \approx 0$.

Similarly, we fit the spreadability data of the 3D hyperuniform medium to the Type I fitting function $\ln[\hat{\mathcal{I}}_1^{\rm ex}(t)]$ and plot the results in Fig. 7(a). We find that $|\delta\hat{\alpha}| = |\hat{\alpha} - 2| \sim 10^{-5}$ and $|\hat{C}_{1/2}|/\sqrt{|\hat{C}_0\hat{C}_1|} \sim 10^{-4} \ll 1$ at the optimal order $n_o = 4$, and thus infer that the spectral density is analytic at the origin with $\alpha = 2$. Figure 7(b) shows the results of the Type III fitting function $\ln[\hat{\mathcal{I}}_3^{\rm ex}(t)]$. The large variance of $\hat{C}_2$ compared to $\hat{C}_0$, $\hat{C}_1$, and $\hat{C}_3$ around the optimal order $n_o = 3$ and the fact that $|\hat{C}_2|/\sqrt{|\hat{C}_1\hat{C}_3|} \sim 10^{-3} \ll 1$ indicates that $C_2 = 0$. The

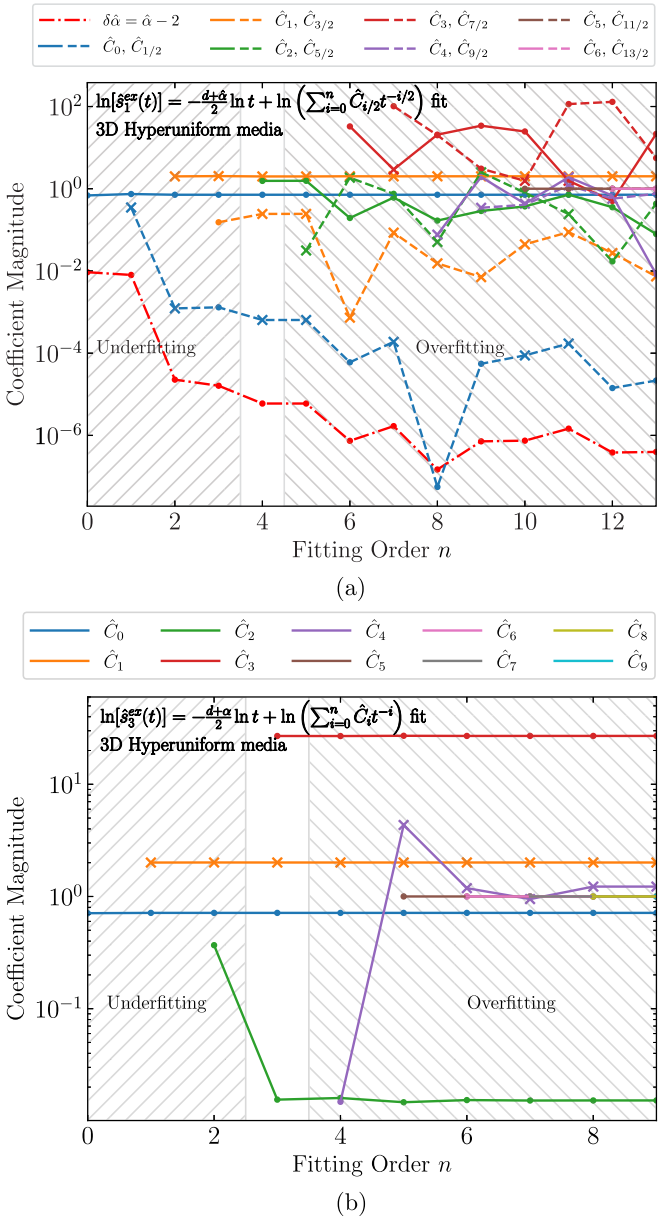


FIG. 7. (a) Type I [Eq. (24)] and (b) Type III [Eq. (30)] fits of $\mathcal{I}^{\rm ex}(t)$ for 3D disordered hyperuniform media [Eq. (C9)]. Positive and negative coefficients are indicated by filled circles and crosses, respectively. The underfitting region ($n < n_o$) and the overfitting region ($n > n_o$) are forward slash and backslash hatched, respectively, while the optimal fitting ($n = n_o$) is left blank.

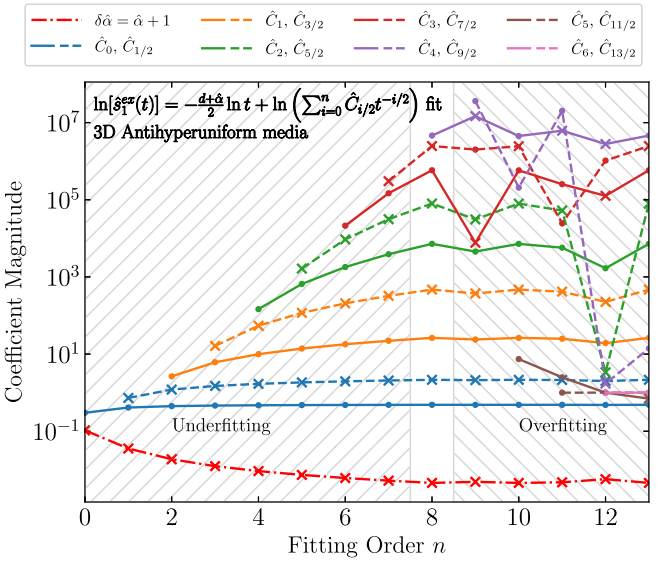
final optimal fit ($n_o = 3$) is given by

$$\mathcal{I}^{\rm ex}(t) = t^{-\frac{d+2}{2}}(\hat{C} + \hat{C}_1 t^{-1} + \hat{C}_2 t^{-2} + \hat{C}_3 t^{-3}), \tag{34}$$

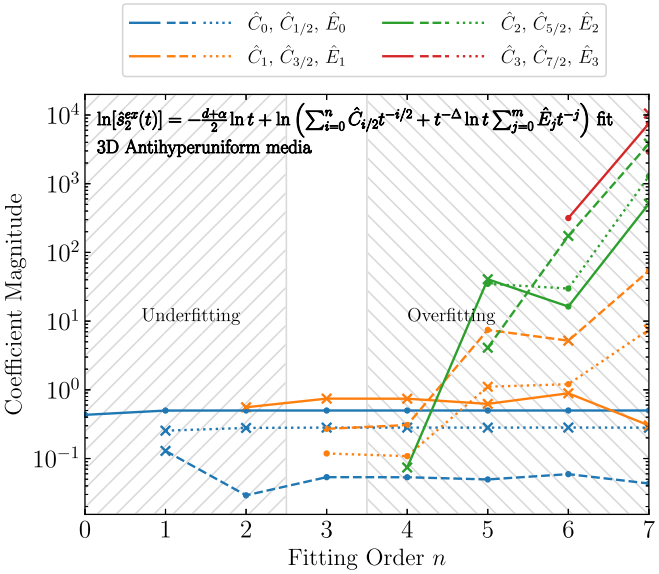
where $|\hat{C}_2|/\sqrt{|\hat{C}_1\hat{C}_3|} \sim 10^{-3} \ll 1$, agreeing perfectly with the exact expansion at the same order

$$\mathcal{I}^{\rm ex}(t) = t^{-\frac{d+2}{2}}(C + C_1 t^{-1} + C_3 t^{-3} + \ldots). \tag{35}$$

In addition to the exponent $\alpha = 2$ and the coefficients $\hat{C}_i$ themselves, we can conclude that the spectral density $\tilde{\chi}_V(k)$ is analytic at the origin up to the order of $k^{\alpha+\beta_3} = k^8$, or equivalently, the moment $M_{d-1+8/2}(\chi_V) = M_6(\chi_V)$ exists, i.e.,



(a)



(b)

FIG. 8. (a) Type I [Eq. (24)] and (b) type II [Eq. (28)] fits of $\mathfrak{z}^{\rm ex}(t)$ for 3D antihyperuniform media [Eq. (C13)]. Positive and negative coefficients are indicated by filled circles and crosses, respectively. The underfitting region ($n < n_o$) and the overfitting region ($n > n_o$) are forward slash and backslash hatched, respectively, while the optimal fitting ($n = n_o$) is left blank.

$\chi_{\rm v}(r) = o(r^{-7})$ as $r \to \infty$. The inferences that $\alpha = 2$ and $|\hat{C}_1| \approx 0$ further imply that $M_{d-1}(\chi_{\rm v}) = 0$ and $M_{d+1}(\chi_{\rm v}) = 0$.

3. *Antihyperuniform media*

Figure 8(a) plots the results of the Type I fits of $\ln[\hat{\mathfrak{z}}_1^{\rm ex}(t)]$, where $|\delta\hat{\alpha}| = |\hat{\alpha}+1|$ continuously decreases down to $\lesssim 10^{-2}$ as the order n increases up to the optimal order $n_o = 8$, implying $\alpha = -1$ within the error range. Since $\alpha = -1$ is negative and odd, the spectral density cannot be analytic at the origin. We then fit the same sample data to the Type II fitting function $\ln[\hat{\mathfrak{z}}_2^{\rm ex}(t)]$ and plot the results in Fig. 8(b). The final optimal fit ($n_o = 3$) is given by

$$\hat{\mathfrak{z}}^{\rm ex}(t) = t^{-\frac{d-1}{2}}(\hat{C} + \hat{C}_{1/2}t^{-1/2} + \hat{C}_1 t^{-1} + \hat{C}_{3/2}t^{-3/2}) + t^{-\frac{d}{2}}\ln t(\hat{E} + \hat{E}_1 t^{-1}), \tag{36}$$

matching the exact expansion truncated at the same order perfectly. In addition to the exponent $\alpha = -1$ and the coefficients $\hat{C}_{i/2}$ and $\hat{E}_i$, we can also infer from the fitting that the autocovariance function behaves like $\chi_{\rm v}(r) \approx r^{-d-\alpha}(K + K_{1/2}r^{-1} + K_1 r^{-2} + K_{3/2}r^{-3}) \sim Kr^{-2}$ as $r \to \infty$.

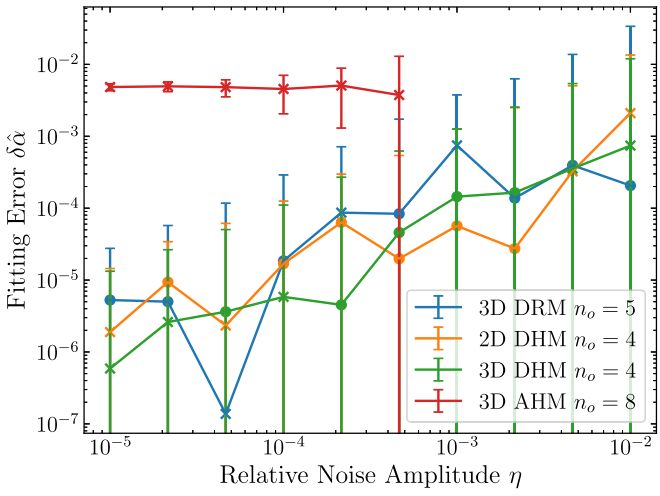


FIG. 9. The fitting error $\delta\hat{\alpha} = \hat{\alpha} - \alpha$ with respect to the relative noise amplitude $\eta = \frac{\sigma}{\mathfrak{z}^{\rm ex}(t_{\rm max})}$ for Debye random media (DRM), disordered hyperuniform media (DHM), and antihyperuniform media (AHM), at their respective optimal order n_o. Positive and negative errors are indicated by filled circles and crosses, respectively.

B. Robustness to random noise

Next, we carry out our analysis by adding random noise to the exact spreadability data to mimic real data. Specifically, we add independent and identically distributed truncated Gaussian noise $\xi(t)$ for each exact spreadability $\mathfrak{z}^{\rm ex}(t)$ datum, i.e., the noise amplitude at each time step is independently sampled from a normal distribution $\mathcal{N}(0,\sigma)$, but truncated to lie in the interval $[-3\sigma, 3\sigma]$. This ensures that the noise at each datum does not exceed three standard deviations from the mean, preventing unrealistic outliers in the simulation. For each σ, we run 50 independent realizations and compute the mean and standard deviation of the fits.

The error of the exponent $\hat{\alpha}$ computed this way for the Type I fit of the examples in the last subsection is shown in Fig. 9. Clearly, the fitting error $\delta\hat{\alpha} = \hat{\alpha} - \alpha$ is about the same order of magnitude as the relative noise amplitude $\eta = \frac{\sigma}{\mathfrak{z}^{\rm ex}(t_{\rm max})}$, i.e., $|\delta\hat{\alpha}| \sim \eta$, unless the *intrinsic error* (without noise) is greater by itself. As can be seen from Fig. 5, the fitting errors of the coefficients essentially synchronize with $\delta\hat{\alpha}$. Therefore, as long as the magnitude of random noise is sufficiently smaller than the normalized excess spreadability, i.e., $\eta = \frac{\sigma}{\mathfrak{z}^{\rm ex}(t_{\rm max})} \ll 1$, it only adds to the fitting error but, importantly, does not affect the fitting procedure and the qualitative conclusions.

For an ensemble of $\mathfrak{z}^{\rm ex}(t)$ data obtained experimentally or numerically, the noise amplitude σ can be estimated by

the standard deviation of the measured $\mathcal{I}^{\rm ex}(t)$ value at the fixed time t. The relative error $\eta = \frac{\sigma}{\mathcal{I}^{\rm ex}(t_{\rm max})}$ can be calculated accordingly and used for error analysis. If η is comparable to the estimated error of $\hat{\alpha}$, the random noise will be the main limitation of the precision. On the other hand, if the estimated $\delta\hat{\alpha}$ is much greater than η, the precision is likely to be improved simply by acquiring data for longer times.

VI. DISCUSSION AND CONCLUSION

In summary, we have developed an improved asymptotic fitting scheme based on our theory of the long-time asymptotics of the normalized excess spreadability $\mathcal{I}^{\rm ex}(t)$ for disordered two-phase random media that are not stealthy hyperuniform. We theoretically classified the asymptotics of all known kinds of two-phase media based on the mathematical properties of their correlation functions $\chi_v(r)$ and $\tilde{\chi}_v(k)$, and numerically show the accuracy of the asymptotic expansion truncated at different orders for the DRM test case. Based on the analyticity properties of $\tilde{\chi}_v(k)$ at the origin [equivalently, the long-distance decay rate of $\chi_v(r)$], we proposed three types of fitting functions for the long-time spreadability fitting. We then demonstrated their ability to accurately extract large-scale two-point correlation information from spreadability data with typical nonhyperuniform (Debye), hyperuniform, and antihyperuniform example models. From our asymptotic fitting procedure, we not only obtained accurate values of the exponent α and the coefficients $C_{\beta_i/2}$ with high precision, but also gained insights into certain mathematical constraints of the correlation functions, including analyticity of $\tilde{\chi}_v(k)$ at the origin, existence of the moment $M_l(\chi_v)$, and long-distance decay rate of $\chi_v(r)$.

Our asymptotic fitting scheme can be readily implemented to analyze real data of $\mathcal{I}^{\rm ex}(t)$ obtained from NMR experiments [17] and numerical simulations [74], and thus helps characterize microstructures in these realistic and practical cases. There are also microstructures of interest requiring separate considerations that are not fully covered in this work, including those whose spectral density cannot be expanded as powers of k at the origin. Examples involve quasicrystalline media due to the dense Bragg peaks in their spectral density [79], and stealthy hyperuniform media characterized by $\tilde{\chi}_v(k) \equiv 0$ for $k < K$. Disordered stealthy hyperuniform materials have unusual structural characteristics (hidden order at large length scales) and physical properties, including desirable photonic and transport properties [82,91]. Generalizing our asymptotic fitting procedure to these exotic microstructures is an open and intriguing problem. Indeed, in future work, we will use our fitting procedure that includes correction terms to estimate the exponent α for quasicrystals, going beyond the use of just the leading term as done in [79].

A useful byproduct of our long-time asymptotic analysis is the two-point Padé approximants of $\mathcal{I}^{\rm ex}(t)$ given by Eq. (20), which approximate the spreadability well for all times. We note that the accuracy of such expressions for all times can be further improved by forming three-point Padé approximants, as noted in Sec. III B. These accurate approximants can then be used to target desired spreadability behaviors at short, intermediate, and long times. This parametrization scheme for the spreadability for all times could be fruitfully applied in the inverse design of microstructures [92] with targeted spreadabilities [90], which can then be fabricated using modern additive manufacturing techniques [93–96] and colloids with tailored interactions [97,98].

ACKNOWLEDGEMENTS

The authors were supported by the Army Research Office under Cooperative Agreement No. W911NF-22-2-0103.

DATA AVAILABILITY

The data that support the findings of this article are not publicly available because they contain commercially sensitive information. The data are available from the authors upon reasonable request.

APPENDIX A: FOURIER TRANSFORM OF POWER-LAW TERMS

When $-d < \Re[\zeta] < 0$, it can be proven that [87,88]

$$\mathcal{F}[r^{-d-\zeta}](\mathbf{k}) \equiv \int_{\mathbb{R}^d} r^{-d-\zeta} e^{-i\mathbf{k}\cdot\mathbf{r}} d\mathbf{r} = G_d(\zeta) k^{\zeta},$$
$$G_d(\zeta) = \frac{\pi^{d/2}\Gamma(-\zeta/2)}{2^{\zeta}\Gamma[(d+\zeta)/2]}. \tag{A1}$$

$G_d(\zeta)k^{\zeta}$ is a meromorphic function on the complex plane, so we can easily extend this result to any $\zeta > -d$ and $\zeta \neq 0, 2, 4, \ldots$ via analytic continuation. Around the poles $\zeta_0 = 2l$, $l = 0, 1, 2, \ldots$, we have the Laurent expansion

$$G_d(\zeta) = \frac{g_{d,l}^{(-1)}}{\zeta - \zeta_0} + g_{d,l}^{(0)} + O[\zeta - \zeta_0],$$
$$k^{\zeta} = k^{\zeta_0}[1 + (\zeta - \zeta_0)\ln k + O[(\zeta - \zeta_0)^2]], \tag{A2}$$

so that

$$G_d(\zeta)k^{\zeta} = \frac{g_{d,l}^{(-1)}k^{\zeta_0}}{\zeta - \zeta_0} + g_{d,l}^{(0)}k^{\zeta_0} + g_{d,l}^{(-1)}k^{\zeta_0}\ln k + O[\zeta - \zeta_0]. \tag{A3}$$

At the poles $\zeta_0 = 0, 2, 4, \ldots$, the finite part gives the meaningful result

$$\mathcal{F}[r^{-d-\zeta_0}](\mathbf{k}) = \text{f.p.}\left[G_d(\zeta_0)k_0^{\zeta}\right] = g_{d,l}^{(0)}k^{\zeta_0} + g_{d,l}^{(-1)}k^{\zeta_0}\ln k, \tag{A4}$$

and it thus contains a generalized power-law term $k^{\zeta_0}\ln k$.

APPENDIX B: PADÉ APPROXIMANT

The Padé approximant technique is a well-known procedure to approximate a function $f(z)$ as a rational function and often provides a superior approximation than its corresponding Taylor series [89]. Specifically, given the Taylor series $f(z) = \sum_{k=0}^{\infty} c_k z^k$, one constructs the rational function $R(z)$ that matches the Taylor series up to that order, i.e.,

$$R(z) = \frac{\sum_{k=0}^{M} a_k z^k}{1 + \sum_{k=1}^{N} b_k z^k}, \tag{B1}$$

such that it obeys the condition

$$R^{(k)}(0) = f^{(k)}(0), \quad k = 0, 1, \ldots, M+N. \tag{B2}$$

We refer to $R(z)$ as the $[M, N]$ Padé approximant of $f(z)$. We can generalize its use by substituting $z \to (x - x_0)^s$.

APPENDIX C: EXACT TWO-PHASE MEDIUM MODELS

1. Debye random media

The Debye random medium (DRM) is a prototypical model of "typical" nonhyperuniform two-phase media [99], for which the autocovariance function

$$\chi_{_V}(r) = \phi_1\phi_2 \exp(-r/a), \tag{C1}$$

and the spectral density

$$\tilde{\chi}_{_V}(k) = \frac{\phi_1\phi_2 2^d \pi^{d-1} a^d}{\omega_{d-1}[1 + (ka)^2]^{(d+1)/2}}, \tag{C2}$$

are known exactly [17]. Without loss of generality, we set $D = a = 1$. The exponential decay of the autocovariance function guarantees the existence of all its moments, i.e., $M_n(\chi_{_V}) = \phi_1\phi_2\Gamma(n+1) < \infty$, and the spectral density is clearly analytic at the origin, i.e., $\tilde{\chi}_{_V}(k) = \sum_{n=0}^{\infty} B_n k^{2n}$ containing only even powers of k. Correspondingly, the asymptotic expansion of $\mathcal{I}^{\rm ex}(t)$ takes the form of

$$\begin{aligned}\mathcal{I}^{\rm ex}(t) &= \sum_{n=0}^{\infty} 2\frac{(-1)^n}{n!}\frac{\Gamma(d+2n)}{\Gamma(d/2)}(4t)^{-d/2-n} \\ &= \sum_{n=0}^{\infty} C_n t^{-d/2-n} \quad (t \to \infty).\end{aligned} \tag{C3}$$

Similarly, we can find its small-t expansion

$$\begin{aligned}\mathcal{I}^{\rm ex}(t) &= \sum_{n=0}^{\infty} \frac{(-1)^n}{n!}\frac{\Gamma(\frac{n+d}{2})}{\Gamma(d/2)}(4t)^{n/2} \\ &= \sum_{n=0}^{\infty} A_n t^{n/2} \quad (t \to 0).\end{aligned} \tag{C4}$$

2. Disordered hyperuniform media

To model hyperuniform two-phase media in $\mathbb{R}^d$, Torquato [82] proposed the following family of autocovariance functions:

$$\chi_{_V}(r) = \phi_1\phi_2 \exp(-r/a)\frac{\cos(qr+\theta)}{\cos\theta}, \tag{C5}$$

where the parameters q and θ are the wave number and phase associated with the oscillations of $\chi_{_V}(r)$, respectively, and a is a correlation length. In the special case in which $\theta = 0$, Torquato showed that the corresponding autocovariance function satisfies all of the necessary realizability conditions and hyperuniformity constraint for $d = 2$ if $(qa)^2 = 1$ and for $d = 3$ if $(qa)^2 = 1/3$. Thus, the spectral densities for $d = 2$ and $d = 3$ are, respectively, given by

$$\frac{\tilde{\chi}_{_V}(k)}{\phi_1\phi_2} = \begin{cases} \frac{2\pi a^2[\sqrt{(ka)^4+4}+4]}{[(ka)^4+4]^{3/2}}[A(k) - A^{-1}(k)] & (d=2), \\ \frac{216\pi a^3[3(ka)^2+8](ka)^2}{[9(ka)^4+12(ka)^2+16]^2} & (d=3), \end{cases} \tag{C6}$$

where $A(k) = \sqrt{\frac{\sqrt{(ka)^4+4}+(ka)^2}{2}}$.

We again set $D = a = 1$. As with DRM, the exponentially decaying autocovariance function (C5) guarantees the existence of all its moments and the analyticity of the spectral density (C6) at the origin. Specifically, we have

$$\frac{M_n(\chi_{_V})}{\phi_1\phi_2} = \begin{cases} \frac{n!}{2^{(n+1)/2}}\cos[(n+1)\pi/4] & (d=2), \\ \frac{n!3^{(n+1)/2}}{2^{n+1}}\cos[(n+1)\pi/6] & (d=3), \end{cases} \tag{C7}$$

and

$$\begin{aligned}\frac{\tilde{\chi}_{_V}(k)}{\phi_1\phi_2} &= \begin{cases} k^2\left(\frac{3\pi}{4} - \frac{35\pi}{128}k^4 + \frac{693\pi}{8192}k^8 + ...\right) & (d=2), \\ k^2\left(\frac{27\pi}{4} - \frac{243\pi}{32}k^2 + \frac{3645\pi}{512}k^6 + ...\right) & (d=3), \end{cases} \\ &= \begin{cases} k^2\sum_{\substack{i=0 \\ i\ \text{even}}}^{\infty} B_i k^{2i} & (d=2), \\ k^2\sum_{\substack{i=0 \\ i\ \text{mod}\ 3\neq 2}}^{\infty} B_i k^{2i} & (d=3). \end{cases}\end{aligned} \tag{C8}$$

Correspondingly, the long-time asymptotic expansion of $\mathcal{I}^{\rm ex}(t)$ is given by

$$\begin{aligned}\mathcal{I}^{\rm ex}(t) &= \begin{cases} t^{-2}\left(\frac{3}{16} - \frac{105}{256}t^{-2} + \frac{10395}{4096}t^{-4} + ...\right) & (d=2), \\ t^{-\frac{5}{2}}\left(\frac{81}{64\sqrt{\pi}} - \frac{3645}{1024\sqrt{\pi}}t^{-1} + ...\right) & (d=3), \end{cases} \\ &= \begin{cases} t^{-\frac{d+2}{2}}\sum_{\substack{i=0 \\ i\ \text{even}}}^{\infty} C_i t^{-i} & (d=2), \\ t^{-\frac{d+2}{2}}\sum_{\substack{i=0 \\ i\ \text{mod}\ 3\neq 2}}^{\infty} C_i t^{-i} & (d=3). \end{cases}\end{aligned} \tag{C9}$$

Note that we have $C_{2i+1} = 0$ for $d = 2$ and $C_{3i+2} = 0$ for $d = 3$ because $M_{d+2i+1}(\chi_{_V}) = 0$ for $d = 2$ and $M_{d+3i+2}(\chi_{_V}) = 0$ for $d = 3$, respectively.

3. Antihyperuniform media

Here, we examine a 3D antihyperuniform model proposed by Torquato [17], which is defined by the autocovariance function

$$\frac{\chi_{_V}(r)}{\phi_1\phi_2} = (1 + r/a)^{-2}, \tag{C10}$$

which meets all known necessary realizability conditions on a valid autocovariance function [82]. The corresponding spectral density is given by

$$\begin{aligned}\frac{\tilde{\chi}_{_V}(k)}{\phi_1\phi_2} = \frac{4\pi a^2}{ka}\{&\mathrm{Ci}(ka)[ka\cos(ka) + \sin(ka)] \\ &+ \mathrm{Ssi}(ka)[ka\sin(ka) - \cos(ka)]\},\end{aligned} \tag{C11}$$

where $\mathrm{Ci}(x) \equiv -\int_x^{\infty} dt\cos(t)/t$ is the cosine integral, $\mathrm{Ssi}(x) \equiv \mathrm{Si}(x) - \pi/2$ is the shifted sine integral, and $\mathrm{Si}(x) \equiv \int_0^x dt\sin(t)/t$ is the sine integral. We see that $\tilde{\chi}_{_V}(k) \sim 2\pi^2 a/k$ in the limit $k \to 0$, which is consistent with the power-law decay a^2/r^2 of the $\chi_{_V}(r)$ in the limit $r \to \infty$.

We again set $D = a = 1$. Clearly, any n-th order moment $M_n(\chi_v)$ for $n \geqslant 1$ is unbounded. This result implies that the spectral density is not analytic at the origin, but this function can be expanded about $k = 0$ as

$$\begin{aligned}\frac{\tilde{\chi}_v(k)}{\phi_1\phi_2} &= \frac{2\pi^2}{k} + 4\pi(2\ln k + 2\gamma_e - 1) - 3\pi^2 k \\ &\quad - \frac{2}{9}\pi k^2(12\ln k + 12\gamma_e - 19) + \frac{5}{12}\pi^2 k^3 + \ldots \\ &= k^{-1}(B + B_{1/2}k + B_1 k^2 + \ldots) \\ &\quad + \ln k(F + F_1 k^2 + F_2 k^4 + \ldots). \end{aligned} \tag{C12}$$

This, in combination with Eq. (1), means that the long-time $\mathcal{I}^{\rm ex}(t)$ can be expanded as

$$\begin{aligned}\mathcal{I}^{\rm ex}(t) &= \frac{1}{2t} + \frac{-\ln t + \gamma_e + 1 - 2\ln 2}{2\sqrt{\pi}t^{3/2}} - \frac{3}{4t^2} \\ &\quad + \frac{2\ln t - 2\gamma_e + 1 + 4\ln 2}{8\sqrt{\pi}t^{5/2}} + \frac{5}{24t^3} + \ldots \\ &= t^{-1}(C + C_{1/2}t^{-1/2} + C_1 t^{-1} + \ldots) \\ &\quad + t^{-3/2}\ln t(E + E_1 t^{-1} + E_2 t^{-2} + \ldots), \end{aligned} \tag{C13}$$

where γ_e is the Euler-Mascheroni constant.

[1] V. J. Wedeen, P. Hagmann, W.-Y. I. Tseng, T. G. Reese, and R. M. Weisskoff, Mapping complex tissue architecture with diffusion spectrum magnetic resonance imaging, Magn. Reson. Med. **54**, 1377 (2005).

[2] D. S. Novikov, J. H. Jensen, J. A. Helpern, and E. Fieremans, Revealing mesoscopic structural universality with diffusion, Proc. Natl. Acad. Sci. USA **111**, 5088 (2014).

[3] H.-H. Lee, A. Papaioannou, D. S. Novikov, and E. Fieremans, In vivo observation and biophysical interpretation of time-dependent diffusion in human cortical gray matter, NeuroImage **222**, 117054 (2020).

[4] D. S. Novikov, E. Fieremans, S. N. Jespersen, and V. G. Kiselev, Quantifying brain microstructure with diffusion MRI: Theory and parameter estimation, NMR Biomed. **32**, e3998 (2019).

[5] D. Wu, K. Jiang, H. Li, Z. Zhang, R. Ba, Y. Zhang, Y.-C. Hsu, Y. Sun, and Y.-D. Zhang, Time-dependent diffusion MRI for quantitative microstructural mapping of prostate cancer, Radiology **303**, 578 (2022).

[6] S. Torquato, *Random Heterogeneous Materials: Microstructure and Macroscopic Properties*, Interdisciplinary Applied Mathematics Vol. 16 (Springer, New York, 2002).

[7] K. R. Brownstein and C. E. Tarr, Importance of classical diffusion in NMR studies of water in biological cells, Phys. Rev. A **19**, 2446 (1979).

[8] B. Sosna, O. Korup, and R. Horn, Probing local diffusion and reaction in a porous catalyst pellet, J. Catal. **381**, 285 (2020).

[9] P. Tahmasebi, Accurate modeling and evaluation of microstructures in complex materials, Phys. Rev. E **97**, 023307 (2018).

[10] R. S. Langer and N. A. Peppas, Present and future applications of biomaterials in controlled drug delivery systems, Biomaterials **2**, 201 (1981).

[11] S. Torquato, Morphology and effective properties of disordered heterogeneous media, Int. J. Solids Struct. **35**, 2385 (1998).

[12] M. A. Klatt, P. J. Steinhardt, and S. Torquato, Phoamtonic designs yield sizeable 3D photonic band gaps, Proc. Natl. Acad. Sci. USA **116**, 23480 (2019).

[13] M. Huang, W. Hu, S. Yang, Q.-X. Liu, and H. P. Zhang, Circular swimming motility and disordered hyperuniform state in an algae system, Proc. Natl. Acad. Sci. USA **118**, e2100493118 (2021).

[14] M. Sahimi, *Heterogeneous Materials I: Linear Transport and Optical Properties* (Springer-Verlag, New York, 2003).

[15] A. K. Sen and S. Torquato, Effective conductivity of anisotropic two-phase composite media, Phys. Rev. B **39**, 4504 (1989).

[16] S. Torquato and J. Kim, Nonlocal effective electromagnetic wave characteristics of composite media: Beyond the quasistatic regime, Phys. Rev. X **11**, 021002 (2021).

[17] S. Torquato, Diffusion spreadability as a probe of the microstructure of complex media across length scales, Phys. Rev. E **104**, 054102 (2021).

[18] S. Prager, Interphase transfer in stationary two-phase media, Chem. Eng. Sci. **18**, 227 (1963).

[19] H. Wang and S. Torquato, Dynamic measure of hyperuniformity and nonhyperuniformity in heterogeneous media via the diffusion spreadability, Phys. Rev. Appl. **17**, 034022 (2022).

[20] S. Torquato and F. H. Stillinger, Local density fluctuations, hyperuniformity, and order metrics, Phys. Rev. E **68**, 041113 (2003).

[21] C. E. Zachary and S. Torquato, Hyperuniformity in point patterns and two-phase random heterogeneous media, J. Stat. Mech. (2009) P12015.

[22] S. Torquato, Hyperuniform states of matter, Phys. Rep. **745**, 1 (2018).

[23] É. Marcotte, F. H. Stillinger, and S. Torquato, Nonequilibrium static growing length scales in supercooled liquids on approaching the glass transition, J. Chem. Phys. **138**, 12A508 (2013).

[24] A. Coniglio, M. P. Ciamarra, and T. Aste, Universal behaviour of the glass and the jamming transitions in finite dimensions for hard spheres, Soft Matter **13**, 8766 (2017).

[25] H. Zhang, X. Wang, J. Zhang, H.-B. Yu, and J. F. Douglas, Approach to hyperuniformity in a metallic glass-forming material exhibiting a fragile to strong glass transition, Eur. Phys. J. E **46**, 50 (2023).

[26] Y. Wang, Z. Qian, H. Tong, and H. Tanaka, Hyperuniform disordered solids with crystal-like stability, Nat. Commun. **16**, 1398 (2025).

[27] S. Mitra, A. D. S. Parmar, P. Leishangthem, S. Sastry, and G. Foffi, Hyperuniformity in cyclically driven glasses, J. Stat. Mech. (2021) 033203.

[28] S. Atkinson, G. Zhang, A. B. Hopkins, and S. Torquato, Critical slowing down and hyperuniformity on approach to jamming, Phys. Rev. E **94**, 012902 (2016).

[29] P. Rissone, E. I. Corwin, and G. Parisi, Long-range anomalous decay of the correlation in jammed packings, Phys. Rev. Lett. **127**, 038001 (2021).

[30] S. Torquato, Structural characterization of many-particle systems on approach to hyperuniform states, Phys. Rev. E **103**, 052126 (2021).
[31] S. Torquato and F. H. Stillinger, Toward the jamming threshold of sphere packings: Tunneled crystals, J. Appl. Phys. **102**, 093511 (2007).
[32] A. Donev, F. H. Stillinger, and S. Torquato, Unexpected density fluctuations in jammed disordered sphere packings, Phys. Rev. Lett. **95**, 090604 (2005).
[33] R. Dreyfus, Y. Xu, T. Still, L. A. Hough, A. G. Yodh, and S. Torquato, Diagnosing hyperuniformity in two-dimensional, disordered, jammed packings of soft spheres, Phys. Rev. E **91**, 012302 (2015).
[34] J. R. Dale, J. D. Sartor, R. C. Dennis, and E. I. Corwin, Hyperuniform jammed sphere packings have anomalous material properties, Phys. Rev. E **106**, 024903 (2022).
[35] M. Florescu, S. Torquato, and P. J. Steinhardt, Designer disordered materials with large, complete photonic band gaps, Proc. Natl. Acad. Sci. USA **106**, 20658 (2009).
[36] L. S. Froufe-Pérez, M. Engel, J. J. Sáenz, and F. Scheffold, Band gap formation and Anderson localization in disordered photonic materials with structural correlations, Proc. Natl. Acad. Sci. USA **114**, 9570 (2017).
[37] W. Man, M. Florescu, K. Matsuyama, P. Yadak, G. Nahal, S. Hashemizad, E. Williamson, P. Steinhardt, S. Torquato, and P. Chaikin, Photonic band gap in isotropic hyperuniform disordered solids with low dielectric contrast, Opt. Express **21**, 19972 (2013).
[38] M. A. Klatt, P. J. Steinhardt, and S. Torquato, Wave propagation and band tails of two-dimensional disordered systems in the thermodynamic limit, Proc. Natl. Acad. Sci. USA **119**, e2213633119 (2022).
[39] O. Christogeorgos, H. Zhang, Q. Cheng, and Y. Hao, Extraordinary directive emission and scanning from an array of radiation sources with hyperuniform disorder, Phys. Rev. Appl. **15**, 014062 (2021).
[40] G. J. Aubry, L. S. Froufe-Pérez, U. Kuhl, O. Legrand, F. Scheffold, and F. Mortessagne, Experimental tuning of transport regimes in hyperuniform disordered photonic materials, Phys. Rev. Lett. **125**, 127402 (2020).
[41] G. Gkantzounis, T. Amoah, and M. Florescu, Hyperuniform disordered phononic structures, Phys. Rev. B **95**, 094120 (2017).
[42] S. Torquato, G. Zhang, and M. De Courcy-Ireland, Hidden multiscale order in the primes, J. Phys. A: Math. Theor. **52**, 135002 (2019).
[43] J. S. Brauchart, P. J. Grabner, and W. Kusner, Hyperuniform point sets on the sphere: Deterministic aspects, Constr. Approx. **50**, 45 (2019).
[44] J. S. Brauchart, P. J. Grabner, W. Kusner, and J. Ziefle, Hyperuniform point sets on the sphere: Probabilistic aspects, Monatsh. Math. **192**, 763 (2020).
[45] S. Torquato, G. Zhang, and M. de Courcy-Ireland, Uncovering multiscale order in the prime numbers via scattering, J. Stat. Mech. (2018) 093401.
[46] M. Björklund and M. Byléhn, Hyperuniformity of random measures on Euclidean and hyperbolic spaces, Math. Ann. **394**, 46 (2026).
[47] M. Byléhn, Hyperuniformity in regular trees, J. Fourier Anal. Appl. **31**, 66 (2025).
[48] S. Ghosh and J. L. Lebowitz, Generalized stealthy hyperuniform processes: Maximal rigidity and the bounded holes conjecture, Commun. Math. Phys. **363**, 97 (2018).
[49] Y. Jiao, T. Lau, H. Hatzikirou, M. Meyer-Hermann, J. C. Corbo, and S. Torquato, Avian photoreceptor patterns represent a disordered hyperuniform solution to a multiscale packing problem, Phys. Rev. E **89**, 022721 (2014).
[50] A. Mayer, V. Balasubramanian, T. Mora, and A. M. Walczak, How a well-adapted immune system is organized, Proc. Natl. Acad. Sci. USA **112**, 5950 (2015).
[51] Y. Zheng, Y.-W. Li, and M. Pica Ciamarra, Hyperuniformity and density fluctuations at a rigidity transition in a model of biological tissues, Soft Matter **16**, 5942 (2020).
[52] W. Hu, L. Cui, M. Delgado-Baquerizo, R. Solé, S. Kéfi, M. Berdugo, N. Xu, B. Wang, Q.-X. Liu, and C. Xu, Causes and consequences of disordered hyperuniformity in global drylands, Proc. Natl. Acad. Sci. USA **122**, e2504496122 (2025).
[53] L.-F. Hou, J. Zhang, G.-Q. Sun, and Z. Jin, Vegetation patterns: Structures and dynamics, CSIAM Trans. Life Sci. **2**, 91 (2026).
[54] D. Hexner, P. M. Chaikin, and D. Levine, Enhanced hyperuniformity from random reorganization, Proc. Natl. Acad. Sci. USA **114**, 4294 (2017).
[55] D. Hexner and D. Levine, Hyperuniformity of critical absorbing states, Phys. Rev. Lett. **114**, 110602 (2015).
[56] Z. Ma and S. Torquato, Hyperuniformity of generalized random organization models, Phys. Rev. E **99**, 022115 (2019).
[57] S. Torquato, G. Zhang, and F. H. Stillinger, Ensemble theory for stealthy hyperuniform disordered ground states, Phys. Rev. X **5**, 021020 (2015).
[58] C. E. Zachary and S. Torquato, Anomalous local coordination, density fluctuations, and void statistics in disordered hyperuniform many-particle ground states, Phys. Rev. E **83**, 051133 (2011).
[59] S. Ganguly and S. Sarkar, Ground states and hyperuniformity of the hierarchical Coulomb gas in all dimensions, Probab. Theory Relat. Fields **177**, 621 (2020).
[60] S. Torquato and J. Kim, Existence of nonequilibrium glasses in the degenerate stealthy hyperuniform ground-state manifold, Soft Matter **21**, 4898 (2025).
[61] S. J. Dawley and S. Torquato, Evolution of various initial many-particle configurations to disordered stealthy hyperuniform ground states, Phys. Rev. E **112**, 045310 (2025).
[62] P. K. Morse, J. Kim, P. J. Steinhardt, and S. Torquato, Generating large disordered stealthy hyperuniform systems with ultrahigh accuracy to determine their physical properties, Phys. Rev. Res. **5**, 033190 (2023).
[63] D. Chen, H. Zhuang, M. Chen, P. Y. Huang, V. Vlcek, and Y. Jiao, Disordered hyperuniform solid state materials, Appl. Phys. Rev. **10**, 021310 (2023).
[64] S. Torquato, A. Scardicchio, and C. E. Zachary, Point processes in arbitrary dimension from fermionic gases, random matrix theory, and number theory, J. Stat. Mech. (2008) P11019.
[65] P. J. D. Crowley, C. R. Laumann, and S. Gopalakrishnan, Quantum criticality in Ising chains with random hyperuniform couplings, Phys. Rev. B **100**, 134206 (2019).

[66] L. D. Abreu, J. M. Pereira, J. L. Romero, and S. Torquato, The Weyl–Heisenberg ensemble: Hyperuniformity and higher Landau levels, J. Stat. Mech. (2017) 043103.

[67] H. Wang, R. Samajdar, and S. Torquato, Correlations in interacting electron liquids: Many-body statistics and hyperuniformity, Phys. Rev. B **110**, 104201 (2024).

[68] D. Chen, R. Samajdar, Y. Jiao, and S. Torquato, Anomalous suppression of large-scale density fluctuations in classical and quantum spin liquids, Proc. Natl. Acad. Sci. USA **122**, e2416111122 (2025).

[69] R. Degl'Innocenti, Y. D. Shah, L. Masini, A. Ronzani, A. Pitanti, Y. Ren, D. S. Jessop, A. Tredicucci, H. E. Beere, and D. A. Ritchie, Hyperuniform disordered terahertz quantum cascade laser, Sci. Rep. **6**, 19325 (2016).

[70] S. Sakai, R. Arita, and T. Ohtsuki, Quantum phase transition between hyperuniform density distributions, Phys. Rev. Res. **4**, 033241 (2022).

[71] C. Vanoni, P. J. Steinhardt, and S. Torquato, Quantifying when hyperuniformity of a many-particle system leads to uniformity across length scales, Phys. Rev. E **112**, 044142 (2025).

[72] P. P. Mitra, P. N. Sen, L. M. Schwartz, and P. Le Doussal, Diffusion propagator as a probe of the structure of porous media, Phys. Rev. Lett. **68**, 3555 (1992).

[73] S. Wilken, A. Chaderjian, and O. A. Saleh, Spatial organization of phase-separated DNA droplets, Phys. Rev. X **13**, 031014 (2023).

[74] M. Skolnick and S. Torquato, Simulated diffusion spreadability for characterizing the structure and transport properties of two-phase materials, Acta Mater. **250**, 118857 (2023).

[75] C. E. Maher, F. H. Stillinger, and S. Torquato, Characterization of void space, large-scale structure, and transport properties of maximally random jammed packings of superballs, Phys. Rev. Mater. **6**, 025603 (2022).

[76] C. E. Maher, Y. Jiao, and S. Torquato, Hyperuniformity of maximally random jammed packings of hyperspheres across spatial dimensions, Phys. Rev. E **108**, 064602 (2023).

[77] C. E. Maher and S. Torquato, Hyperuniformity scaling of maximally random jammed packings of two-dimensional binary disks, Phys. Rev. E **110**, 064605 (2024).

[78] K. J. Wiese, Hyperuniformity in the Manna model, conserved directed percolation and depinning, Phys. Rev. Lett. **133**, 067103 (2024).

[79] A. Hitin-Bialus, C. E. Maher, P. J. Steinhardt, and S. Torquato, Hyperuniformity classes of quasiperiodic tilings via diffusion spreadability, Phys. Rev. E **109**, 064108 (2024).

[80] P. Debye and A. M. Bueche, Scattering by an inhomogeneous solid, J. Appl. Phys. **20**, 518 (1949).

[81] P. Debye, H. R. Anderson, Jr., and H. Brumberger, Scattering by an inhomogeneous solid. II. The correlation function and its application, J. Appl. Phys. **28**, 679 (1957).

[82] S. Torquato, Disordered hyperuniform heterogeneous materials, J. Phys.: Condens. Matter **28**, 414012 (2016).

[83] H. E. H. E. Stanley, *Introduction to Phase Transitions and Critical Phenomena* (Oxford University Press, New York, 1987).

[84] J. J. Binney, N. J. Dowrick, A. J. Fisher, and M. E. J. Newman, *The Theory of Critical Phenomena: An Introduction to the Renormalization Group* (Oxford University Press, Oxford, England, 1992).

[85] S. Torquato and H. Wang, Precise determination of pair interactions from pair statistics of many-body systems in and out of equilibrium, Phys. Rev. E **106**, 044122 (2022).

[86] J.-P. Hansen and I. R. McDonald, *Theory of Simple Liquids* (Academic Press, Oxford, 2013).

[87] L. Hörmander, *The Analysis of Linear Partial Differential Operators I*, Classics in Mathematics (Springer Berlin Heidelberg, Berlin, Heidelberg, 2003).

[88] R. P. Kanwal, *Generalized Functions* (Birkhäuser Boston, Boston, MA, 2004).

[89] G. A. J. Baker, *Essentials of Padé approximants* (Academic Press, New York, 1975).

[90] W. Shi, Y. Jiao, and S. Torquato, Three-dimensional construction of hyperuniform, nonhyperuniform, and antihyperuniform disordered heterogeneous materials and their transport properties via spectral density functions, Phys. Rev. E **111**, 035310 (2025).

[91] G. Zhang, F. H. Stillinger, and S. Torquato, Transport, geometrical, and topological properties of stealthy disordered hyperuniform two-phase systems, J. Chem. Phys. **145**, 244109 (2016).

[92] S. Torquato, Inverse optimization techniques for targeted self-assembly, Soft Matter **5**, 1157 (2009).

[93] B. Bhushan and M. Caspers, An overview of additive manufacturing (3D printing) for microfabrication, Microsyst. Technol. **23**, 1117 (2017).

[94] S. F. S. Shirazi, S. Gharehkhani, M. Mehrali, H. Yarmand, H. S. C. Metselaar, N. Adib Kadri, and N. A. A. Osman, A review on powder-based additive manufacturing for tissue engineering: Selective laser sintering and inkjet 3D printing, Sci. Technol. Adv. Mater. **16**, 033502 (2015).

[95] J. R. Tumbleston, D. Shirvanyants, N. Ermoshkin, R. Janusziewicz, A. R. Johnson, D. Kelly, K. Chen, R. Pinschmidt, J. P. Rolland, A. Ermoshkin, E. T. Samulski, and J. M. DeSimone, Continuous liquid interface production of 3D objects, Science **347**, 1349 (2015).

[96] K. V. Wong and A. Hernandez, A review of additive manufacturing, Int. Scholarly Res. Not. **2012**, 208760 (2012).

[97] D. Chen, E. Lomba, and S. Torquato, Binary mixtures of charged colloids: A potential route to synthesize disordered hyperuniform materials, Phys. Chem. Chem. Phys. **20**, 17557 (2018).

[98] Z. Ma, E. Lomba, and S. Torquato, Optimized large hyperuniform binary colloidal suspensions in two dimensions, Phys. Rev. Lett. **125**, 068002 (2020).

[99] C. L. Y. Yeong and S. Torquato, Reconstructing random media, Phys. Rev. E **57**, 495 (1998).